



HAL
open science

Two-dimensional numerical simulation of chimney fluidization in a granular medium using a combination of discrete element and lattice Boltzmann methods

Jeff Ngoma, Pierre Philippe, Stéphane Bonelli, Farhang Radjai, Jean-Yves Delenne

► **To cite this version:**

Jeff Ngoma, Pierre Philippe, Stéphane Bonelli, Farhang Radjai, Jean-Yves Delenne. Two-dimensional numerical simulation of chimney fluidization in a granular medium using a combination of discrete element and lattice Boltzmann methods. *Physical Review E*, 2018, 97 (5), pp.052902. 10.1103/PhysRevE.97.052902. hal-02095646

HAL Id: hal-02095646

<https://hal.science/hal-02095646>

Submitted on 10 Apr 2019

HAL is a multi-disciplinary open access archive for the deposit and dissemination of scientific research documents, whether they are published or not. The documents may come from teaching and research institutions in France or abroad, or from public or private research centers.

L'archive ouverte pluridisciplinaire **HAL**, est destinée au dépôt et à la diffusion de documents scientifiques de niveau recherche, publiés ou non, émanant des établissements d'enseignement et de recherche français ou étrangers, des laboratoires publics ou privés.

Two-dimensional numerical simulation of chimney fluidization in a granular medium using a combination of discrete element and lattice Boltzmann methods

Jeff Ngoma,¹ Pierre Philippe,¹ Stéphane Bonelli,¹ Farhang Radjai,^{2,3} and Jean-Yves Delenne⁴

¹IRSTEA, UR RECOVER, 3275 route de Cézanne, CS 40061, Aix-en-Provence, F-13182, France

²LMGC, CNRS University of Montpellier, 163 rue Auguste Broussonnet, Montpellier, F-34090, France

³Multiscale Material Science for Energy and Environment, CNRS/MIT/AMU Joint Laboratory, Massachusetts Institute of Technology, 77 Massachusetts Avenue, Cambridge, Massachusetts 02139, USA

⁴IATE, INRA, CIRAD, Montpellier SupAgro, Université de Montpellier, 2 place Pierre Viala, Montpellier, F-34060, France



(Received 13 February 2018; published 10 May 2018)

We present here a numerical study dedicated to the fluidization of a submerged granular medium induced by a localized fluid injection. To this end, a two-dimensional (2D) model is used, coupling the lattice Boltzmann method (LBM) with the discrete element method (DEM) for a relevant description of fluid-grains interaction. An extensive investigation has been carried out to analyze the respective influences of the different parameters of our configuration, both geometrical (bed height, grain diameter, injection width) and physical (fluid viscosity, buoyancy). Compared to previous experimental works, the same qualitative features are recovered as regards the general phenomenology including transitory phase, stationary states, and hysteretic behavior. We also present quantitative findings about transient fluidization, for which several dimensionless quantities and scaling laws are proposed, and about the influence of the injection width, from localized to homogeneous fluidization. Finally, the impact of the present 2D geometry is discussed, by comparison to the real three-dimensional (3D) experiments, as well as the crucial role of the prevailing hydrodynamic regime within the expanding cavity, quantified through a cavity Reynolds number, that can presumably explain some substantial differences observed regarding upward expansion process of the fluidized zone when the fluid viscosity is changed.

DOI: [10.1103/PhysRevE.97.052902](https://doi.org/10.1103/PhysRevE.97.052902)

I. INTRODUCTION

Particle fluidization is commonly implemented in a large variety of industrial processes including drying [1], biomass gasification [2,3], and elutriation [4,5]. Most of these applications, and an overwhelming majority of the related literature, involve homogeneous fluidization, generally induced by a uniform upward fluid flow. By contrast, few studies have focused on partial fluidization generated by a localized fluid flow even if several industrial processes are directly concerned with such situations as spouted beds [6,7], tapered beds [8], or specific fluidizers designed for maintenance of navigable waterways and sand bypassing [9]. The existence of *fluid escape structures* is also widely encountered in natural geological formations [10–14] and in some undesired problematic cases including channelling in fluidized reactors [15] and expansion, possibly leading to collapse, of underground cavities in the vicinity of a leaking buried pipeline [16] and in the foundation of an embankment dam subject to seepage flow [17,18]. That last example is of high relevance in the general context of dyke and dam safety since one of the two main threats of such hydraulic structures is internal erosion, a generic term covering four identified mechanisms of soil erosion within an embankment dam, or its foundations, under the action of infiltration water flows [17,18]. Among these mechanisms of internal erosion, backward erosion denotes a regressive pipe expansion process within a sandy foundation of a levee, whose precursory stage is precisely a localized fluidization, more commonly called sand boiling, located at or not far behind the downstream side of the dike [19–21].

In all these situations of partial fluidization within a granular material, the common scientific issue deals with the interactive coupling between an interstitial fluid flow and a surrounding particle matrix which, at an intermediate scale, can be either a static pack, with an internal stress capable of withstanding the fluid flow loading, or a concentrated suspension where the particulate medium gets locally destabilized and fluidized by the fluid flow. Moreover, any structural change within the granular material affects the permeability and modifies in turn the fluid flow in a direct and complex feedback loop. In particular, it is both a challenging fundamental question and a practical issue to determine the location of the dynamical frontiers between these static and fluidized zones as well as their evolution in time and space, especially in the immediate vicinity of the localized fluidization onset, at a rather moderate fluid flow rate. Several previous studies have focused more or less distantly on this topic but there is still work to be done for an overall and satisfactory understanding of the problem at the grain scale.

From an experimental perspective, most investigations were based on a quasi-2D geometry in narrow cells, or at a transparent wall, to allow for direct visual observation, either for a liquid fluidized case [13,22–25] or more often for fluidization by a gas [14,26–30], even with a cohesive material [31]; some of these studies aimed exclusively at validating a numerical model [26,29,30]. However, huge wall effects may occur in such confined configurations and they are likely to interfere with the fluidization process. To overcome this difficulty and minimize boundary effects, some other experiments have used a real

3D geometry but at the expense of the visualization, which remained limited to the top surface of the particle bed and/or to a lateral window, again for either gas fluidization [12] or liquid fluidization [23,25,32–34]. More recently, some noninvasive volume probing techniques have been implemented, such as positron emission particle tracking and electrical capacitance tomography in a study focusing on bed elevation in steady spout-fluidized beds [30] and magnetic resonance imaging for the identification of a fluidized chimney during its formation [35,36]. A direct observation of localized fluidization through an artificial granular medium has also been obtained [37,38], combining two optical techniques, refractive index matching and planar laser induced fluorescence [38–40]. The available experimental data and phenomenological observations given in Ref. [38] about the transient expansion of a fluidized cavity, its final steady state, and some related hysteresis effects, also studied in Ref. [36], provided valuable benchmarks to validate the numerical modeling detailed in the present study.

Many numerical models have been developed so far to simulate fluidized beds: continuous modeling based on the two-phase theory [41] or, more recently, methods combining discrete and continuous approaches for the solid and fluid phases respectively [41,42]. Nevertheless, only a few of these studies have focused on localized fluidization. Apart from a very recent work based on Computational Fluid Dynamics (CFD) computation including granular kinetic theory with Eulerian approach [43], all other previous numerical investigations used a discrete particle approach to model related systems such as multiple spout-fluidized beds [29], gas-fluidized bed by DEM-CFD algorithm [44], fluidization of a cohesionless particulate bed by a localized fluid influx [45,46], or even partial fluidization of a cohesive soil layer by DEM-LBM simulation [47,48]. As in these two latter studies, combining the discrete element method and the lattice Boltzmann method appears to be a highly efficient strategy for simulating fluid-grain coupling in relation to soil mechanic issues [49–51] including porous flow [52], immersed granular flows [53,54], and soil erosion [55–57]. Building on some previous works of DEM-LBM modeling [54,58], the present study proposed a 2D modeling of partial fluidization inside a cohesionless granular sample by an upward fluid flow injected at the bottom of the grain layer with a variable width. Part of the numerical results were directly compared to previous experiments carried out in similar configurations [22–24,34,37,38].

The paper is organized as follows. First, the principles of the numerical methods are introduced in Sec. II, including brief descriptions of the lattice Boltzmann method (Subsec. II A) and the discrete element method (Subsec. II B), followed by some details about how both methods are coupled together in the present 2D geometry (Subsec. II C), and finally some validation tests (Subsec. II D). Then, Sec. III focuses on the application of the model to the situation of localized fluidization, successively presenting the simulation configuration, the parameters under study, and the protocol of the numerical experiments to be carried out. The numerical results obtained from a comprehensive parametric analysis, notably by variation of the fluid flow injection width, are next detailed in Sec. IV, including successively the different steady-state regimes of fluidization and some related hysteresis effects when the flow rate is decreased (Subsec. IV A), the determination of the onset

for chimney fluidization and the subsequent transient regime duration (Subsec. IV B), and finally the influence of injection size on the fluidization threshold (Subsec. IV C). All these results are systematically discussed in the light of previous experimental, theoretical, and numerical data. A summary of successful comparisons and also substantial differences is presented in Sec. V, pointing out some limitations of our 2D modeling as well as the dependence of the chimney fluidization behavior to fluid flow injection size and hydrodynamic regime within the fluidized cavity. Finally, Sec. VI gives an overview of the present study and suggests some conclusions and perspectives.

II. DESCRIPTION OF NUMERICAL METHODS

In the following sections, a brief introduction to the two numerical methods is given. For more detailed description, we refer to the literature cited.

A. Lattice Boltzmann method (LBM)

1. Principles of the LBM

The lattice Boltzmann method is a relatively new numerical approach to simulate quasi-incompressible fluid flows that can be used as an alternative to the more traditional computational fluid dynamics (CFD) methods based on a direct resolution of the Navier-Stokes equations. Historically, the LBM originated as an extension of lattice gas cellular automata models and kept the basic idea that the fluid is modeled as a large number of small particles located at the nodes of a regular lattice [59,60]. For the general purpose of tracking the time evolution of the population of fluid particles, a distribution function $f(\vec{x}, \vec{c}, t)$ was introduced by Boltzmann as the probability density to find a particle at the position \vec{x} , with the velocity \vec{c} at the given time t . Then the fluid dynamics can be simply described by the Boltzmann equation which, once discretized on a regular lattice using a finite set of directional vectors \vec{e}_i and associated velocity vectors $\vec{c}_i = c\vec{e}_i$ reads

$$\frac{\partial f_i}{\partial t} + \vec{c}_i \cdot \vec{\nabla} f_i = \Omega_i(f), \quad (1)$$

where $f_i(\vec{x}, \vec{c}_i, t)$ denotes the distribution function in direction i , Ω_i is the corresponding collision operator, and c is the so-called lattice velocity.

The LBM uses a specific time and space discretization of Eq. (1) given by [59,61,62]

$$f_i(\vec{x} + \vec{c}_i \Delta t, t + \Delta t) - f_i(\vec{x}, t) = \Omega_i(f), \quad (2)$$

where the characteristic lattice velocity c and the time step Δt are chosen so that $c = h/\Delta t$, with h denoting the lattice grid spacing. Consequently, during each time step, a fluid particle is allowed either to stay at rest ($\vec{c}_0 = \vec{0}$) or to move to one of the neighboring nodes along the direction \vec{e}_i . Note also that $h = \Delta t = c = 1$ in lattice units (space and time). In the literature, the LB formulation is often described in lattice units where all the variables can be dimensionless, thereby offering an implementation advantage.

For the present study, the D2Q9 lattice scheme was used. In this scheme, the space is divided into square domains where each node has a set of distribution functions f_i , representing

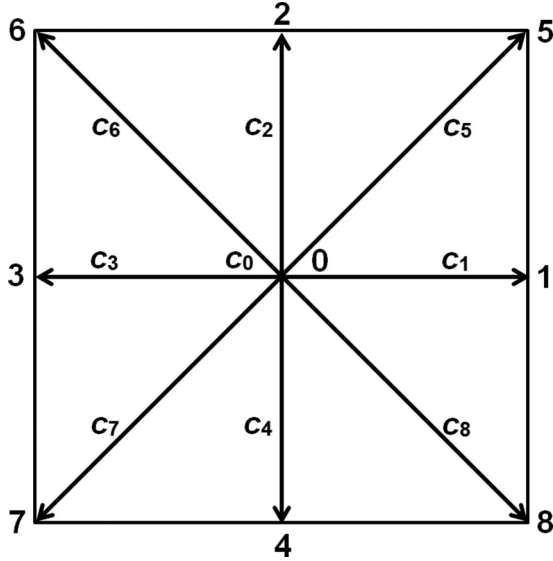


FIG. 1. The LBM cell of the D2Q9 lattice showing the direction of each one of the nine discrete velocities.

the density of fluid particles going through one of the nine discrete velocities \vec{c}_i shown in Fig. 1. The discrete velocities are given by

$$\vec{c}_i = c \begin{cases} (0,0) & i = 0 \\ (\cos[-1]\pi/2, \sin[(i-1)\pi/2]) & i = 1-4, \\ (\cos[(2i-9)\pi/4], \sin[(2i-9)\pi/4]) & i = 5-8. \end{cases} \quad (3)$$

At each lattice node, the macroscopic fluid quantities such as the density ρ and the velocity \vec{u} can be recovered from the moments of the distribution functions. In lattice units, we have

$$\rho = \sum_{i=0}^8 f_i, \rho \vec{u} = \sum_{i=0}^8 f_i \vec{e}_i. \quad (4)$$

To determine the fluid pressure p , the fluid is assumed to be slightly compressible. The pressure is then derived directly from the density using the following state equation for an ideal gas:

$$p = c_s^2 \rho, \quad (5)$$

where c_s is the sound celerity and is defined in the D2Q9 model as $c_s = c/\sqrt{3}$.

More or less sophisticated collision models can be introduced to solve Eq. (2) provided that conservation laws are satisfied. A simple and very popular model was originally proposed by Bhatnagar *et al.* [59,63] and is referred to as the BGK or single-relaxation-time model. It is based on the assumption that the distribution function $f_i(\vec{x}, t)$ tends to relax toward its equilibrium value $f_i^{\text{eq}}(\vec{x}, t)$ with a characteristic time τ , as reflected in the following expression used for the collision operator Ω_i :

$$\Omega_i = -\frac{1}{\tau} [f_i(\vec{x}, t) - f_i^{\text{eq}}(\vec{x}, t)]. \quad (6)$$

The equilibrium distribution function $f_i^{\text{eq}}(\vec{x}, t)$ can be written as a function of the macroscopic quantities [59,64]:

$$f_i^{\text{eq}}(\rho, \vec{u}) = \omega_i \rho \left[1 + 3(\vec{e}_i \cdot \vec{u}) + \frac{9}{2}(\vec{e}_i \cdot \vec{u})^2 - \frac{3}{2}\vec{u}^2 \right], \quad (7)$$

where the weighting factors ω_i for the D2Q9 model are assigned as follows: $\omega_i = 4/9$ for $\|\vec{c}_i\| = 0$, $\omega_i = 1/9$ for $\|\vec{c}_i\| = 1$, and $\omega_i = 1/36$ for $\|\vec{c}_i\| = \sqrt{2}$. In practice, Eq. (2) is usually solved in two steps, namely a collision step and a streaming step, as detailed below for the BGK scheme:

Collision step:

$$f_i(\vec{x}, t^+) = f_i(\vec{x}, t) - \frac{1}{\tau} [f_i(\vec{x}, t) - f_i^{\text{eq}}(\vec{x}, t)], \quad (8)$$

Streaming step:

$$f_i(\vec{x} + \vec{c}_i \Delta t, t + \Delta t) = f_i(\vec{x}, t^+), \quad (9)$$

where t^+ denotes the postcollision time step.

The collision phase accounts for the interactions between fluid particles, which commonly result in relaxation toward an equilibrium distribution. With the particles being in motion, the propagation phase consists of spreading the postcollision distribution functions over the neighboring lattice nodes along different discrete velocity directions \vec{e}_i .

The highly attractive benefit of the BGK collision model is mostly its ability to lead to Navier-Stokes equations by a Chapman-Enskog expansion [51,59,65,66], provided that the fluid incompressibility condition is almost satisfied. In this sense, the LBM is equivalent to solving the Navier-Stokes equations. Intrinsically, and notably regarding Eq. (5), the LBM modeling of a fluid flow requires the existence of a slight spatial density variation. As a consequence, an approximate incompressibility situation can be achieved only under the condition that the Mach number $\text{Ma} = u_{\text{max}}/c$ is small, i.e., $\text{Ma} \ll 1$, and in practice $\text{Ma} \leq 0.1$ [57,66], with u_{max} being the maximum velocity in the flow. Then, the following relation holds between the relaxation time τ and the kinematic viscosity ν_f of the fluid:

$$\tau = \frac{1}{2} + \frac{3\nu_f}{hc}. \quad (10)$$

The BGK model is, however, based on a unique relaxation time τ and consequently all dynamic variables evolve with the same characteristic time. This shortcoming may cause numerical instabilities when the relaxation time parameter τ is close to $1/2$. Several alternative collision models exist, which retain the capability to simulate fluid flows obeying incompressible Navier-Stokes equations and whose numerical solutions are more robust. Among them, the multi-relaxation-time (MRT) model [67–69], which has been used for the present simulations with the D2Q9 model, consists in evaluating nine different variables, or moments m_i , at every fluid node, defined directly from the distribution functions f_i through a matrix of moments M . For each of these moments, a relaxation collision step is implemented similarly to Eq. (8) with a specific relaxation time τ_i and an equilibrium value m_i^{eq} which can be expressed as a function of ρ and \vec{u} . The same relation as Eq. (10) holds for the kinematic viscosity with $\tau = \tau_7 = \tau_8$. More details about the MRT model in 2D LBM simulation can be found in Ref. [68].

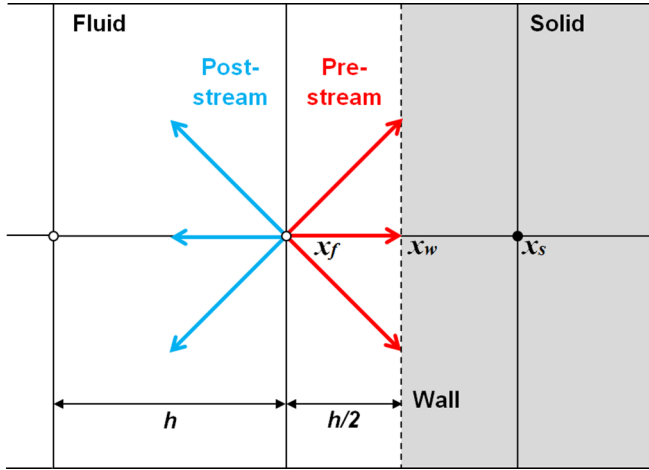


FIG. 2. Bounce-back rule for stationary solid wall.

2. Fluid domain boundary conditions

Classical and commonly used boundary conditions were implemented in this study. In the LB method, the pressure or velocity boundary conditions cannot be directly imposed since they derive from the particle distribution functions f_i . Consequently, the distribution functions must be defined to set the desired values of the hydrodynamic quantities at the boundary nodes. Here we chose to use pressure and velocity boundary conditions similar to the ones proposed by Zou and He [70], based on a bounce-back scheme of the nonequilibrium part of distribution functions. The pressure boundary condition is imposed in LB by specifying a fluid density at the pressure boundary and the velocity boundary condition can be given in a similar way [59,60,70]. Other boundary conditions, such as periodic and free-slip conditions, can be found, for instance, in Refs. [60,71–75].

The nonslip boundary condition between the fluid and a stationary solid wall is imposed through the so-called bounce-back rule. In its simplest version, the solid-fluid interface is assumed to be located exactly at the middle of the boundary link, between the fluid boundary nodes and solid boundary nodes (see Fig. 2). In this work, we used the halfway bounce-back scheme for the sake of simplicity and reducing the computation cost. The solid nodes are inactive except those belonging to the boundary which reflect any incoming distribution $f_i(\vec{x}_f, t)$ during the streaming step from a liquid node according to the following relation:

$$f_{-i}(\vec{x}_f, t + \Delta t) = f_i(\vec{x}_f, t^+), \quad (11)$$

where, by convention, $-i$ denotes the opposite direction of i , and $f_i(\vec{x}_f, t^+)$ is the postcollision distribution function at the fluid node [see Eq. (9)].

B. Discrete element method

The discrete element method (DEM) was initially developed by Cundall and Strack [76] to deal with problems in rock mechanics. Though this method was originally proposed to predict the behavior of soil, it has been found to be applicable to many other phenomena concerned with granular materials. Today, it is becoming widely accepted as an effective alter-

native solution to address engineering problems. The DEM treats bulk solid as a system of distinct interacting bodies. Each particle is identified separately having its own mass, velocity, and contact properties. The particles are assumed to be rigid, but a slight overlap is allowed during a collision. When a contact occurs between two particles, a local constitutive law determines the interparticle contact forces and consequently the resulting motions of the particles involved in the contact.

The particle's motion can be described through Newton's equations, boundaries, or external forces such as hydrodynamic forces. If all forces \vec{F}_i acting on a particle i by other particles or the fluid are known, the problem is reduced to the integration of the equations of translational and rotational particle motions given by

$$m_i \frac{d^2 \vec{r}_i}{dt^2} = \vec{F}_i + m_i \vec{g}, \quad (12)$$

$$I_i \frac{d\vec{\omega}_i}{dt} = \vec{T}_i, \quad (13)$$

with the mass m_i of particle i , its position \vec{r}_i , its moment of inertia I_i , its angular velocity $\vec{\omega}_i$, the acceleration due to volume forces like gravity \vec{g} , and the total force and torque \vec{F}_i and \vec{T}_i .

For each particle, Newton's laws can be solved numerically by explicit numerical integration. The standard velocity-Verlet scheme is used here. The total force \vec{F}_i and torque \vec{T}_i acting on the particle i are given by

$$\vec{F}_i = \vec{F}_i^c + \vec{F}_i^h \quad (14)$$

and

$$\vec{T}_i = \vec{T}_i^c + \vec{T}_i^h, \quad (15)$$

where \vec{F}_i^c is the total contact force with the neighboring particles and \vec{F}_i^h is the hydrodynamic force applied on the particle, as detailed in the next section. \vec{T}_i^c and \vec{T}_i^h denote the torques generated by the contact and hydrodynamic actions, respectively.

The contact force models commonly used in the DEM are discussed in detail in the literature [76–82]. The contact force \vec{F}_{ij}^c between two neighboring particles i and j results from elastic, viscous, and frictional resistances which can be modeled as a spring, a dashpot, and a shear slider respectively. The spring deals with elastic interaction law while the dashpot models energy dissipation at the contact. The shear slider accounts for the frictional force at the contact point (see Fig. 3).

More precisely, the contact force \vec{F}_{ij}^c between particles i and j is composed of normal and tangential components:

$$\vec{F}_{ij}^c = F_{ij}^n \vec{n}_{ij} + F_{ij}^t \vec{t}_{ij}. \quad (16)$$

The contact forces exist only when the two particles overlap. For circular particles, it requires the following condition for the normal overlap δ_{ij}^n :

$$\delta_{ij}^n = \frac{1}{2}(d_i - d_j) - |\vec{r}_i - \vec{r}_j| \cdot \vec{n} \geq 0, \quad (17)$$

where δ_{ij}^n is the relative displacement between the two particles i and j in the normal direction; d_i , d_j , \vec{r}_i , and \vec{r}_j are the radius and position vector of particles i and j respectively; and the unit vector \vec{n}_{ij} is defined by $\vec{n}_{ij} = (\vec{r}_i - \vec{r}_j) / \|\vec{r}_i - \vec{r}_j\|$.

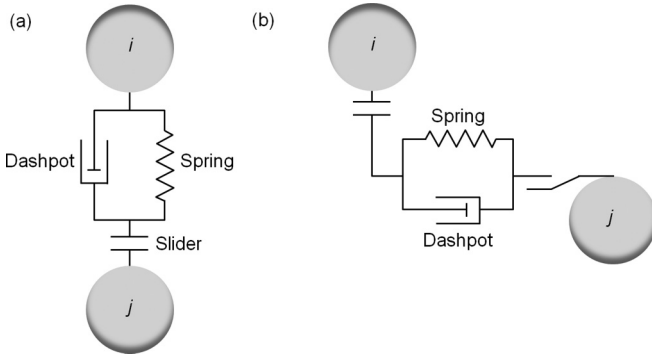


FIG. 3. Models of a contact force between a particles i and a particle j : (a) normal force and (b) tangential force.

The normal component F_{ij}^n of the contact force is modeled as a linear function of the overlap δ_{ij}^n and of the relative normal velocity between the particles $v_{ij}^n = (\vec{v}_i - \vec{v}_j) \cdot \vec{n}$:

$$F_{ij}^n = -k_n \delta_{ij}^n - \gamma_n v_{ij}^n, \quad (18)$$

where k_n is the normal spring stiffness and γ_n is the normal coefficient of viscous dissipation.

The tangential component F_{ij}^t of the contact force is calculated using a viscous-regularized Coulomb model, the details of which can be found in literature [76–83], and reads

$$F_{ij}^t = -\min(K_t v_{ij}^t, \mu F_{ij}^n) \text{sgn}(v_{ij}^t), \quad (19)$$

where K_t is the so-called coefficient of regularization, $v_{ij}^t = (\vec{v}_i - \vec{v}_j) \cdot \vec{t}$ is the tangential velocity, and μ is the friction coefficient.

The time step used in the time integration of Newton's equations given in Eqs. (12) and (13) should be appropriately selected to describe the particle motion correctly. In particular, to ensure numerical stability, it should be below a critical value that is the oscillation period of the spring-mass system used to model two contacting particles [83,84]:

$$\Delta t_{\text{cr}} = 2\pi \sqrt{m/k_n}, \quad (20)$$

where m is the smallest particle mass.

Note that the normal coefficient γ_n of viscous dissipation is related to the coefficient of restitution e [81]:

$$\gamma_n = \frac{-2 \ln e \sqrt{k_n m}}{\sqrt{(\ln e)^2 + (\pi)^2}}. \quad (21)$$

The computation time step of particle motion used in our DEM simulations is consequently taken as $\Delta t_D = \lambda \Delta t_{\text{cr}}$ with a time step factor λ chosen around 0.1 to ensure stability and reasonable accuracy of the solution [47,85,86] as well as acceptable computation duration.

C. LBM and its coupling with DEM

The coupling between the LB and DE methods is a powerful numerical tool to efficiently describe the physical behavior of fluid dynamics in pore scale and intensive fluid-structure interaction. It requires the exchange of information from one method to the other. Hydrodynamic forces and torques are deduced from the LB computation and used in the DE

framework to compute new positions and velocities of solid particles, which in turn define the new boundary conditions. In literature, more details on the coupled DEM-LBM technique and its applications can be found [47,48,51,52,85–90]. Here, we give only the details necessary for understanding the numerical model.

For the particle transport problems concerned, it is very important to correctly model the interactions between fluid and particles in order to capture and explain essential physical behavior of the system. This requires a physically exact nonslip boundary condition to be imposed at fluid-solid interface. For a stationary solid surface, the nonslip condition can be easily imposed by applying bounce-back rule as already mentioned earlier. When the solid boundary is moving, it is more difficult to model the interaction between the fluid and moving particles. The immersed moving boundary (IMB) scheme proposed by Noble and Torczynski [91] is adopted in the present work. This scheme treats the particles as moving solid boundaries in fluid flows. It provides more accurate and smooth lattice representation of solid particles to reduce the fluctuation of the computed hydrodynamic forces and torques acting on a moving particle, as well as the modification of the LBM equation at the lattice nodes fully or partially covered by a moving solid particle to enforce the nonslip condition at the fluid-solid interface. The detailed implementation of this coupling scheme was illustrated in Refs. [47,52,57,58,72,85–87,92–94].

In the present work, the interpolated bounce-back boundary conditions proposed by Bouzidi *et al.* [87] is considered. The equations of linear interpolation are

$$f_{-i}(\vec{x}_f, t + \Delta t) = 2\Delta f_i(\vec{x}_f, t) + (1 - 2\Delta) f_i(\vec{x}_f - \vec{c}_i, t^+) + 6\omega_i \rho \vec{c}_i \vec{u}_w / c^2, \Delta < 1/2, \quad (22)$$

$$f_{-i}(\vec{x}_f, t + \Delta t) = \frac{1}{2\Delta} f_i(\vec{x}_f, t) + \frac{(1 - 2\Delta)}{2\Delta} f_i(\vec{x}_f - \vec{c}_i, t^+) + \frac{3}{\Delta} \omega_i \rho \vec{c}_i \vec{u}_w / c^2, \Delta \geq 1/2, \quad (23)$$

where $\Delta = \|\vec{x}_f - \vec{x}_w\| / \|\vec{x}_f - \vec{x}_c\|$ is the distance of the fluid node from the boundary surface, normalized by the grid spacing, and where the local velocity of the wall \vec{u}_w is given as

$$\vec{u}_w = \vec{u}_c + \omega \times (\vec{x} + \vec{c}_i \Delta t / 2 - \vec{x}_c) \quad (24)$$

in which \vec{u}_c and ω are the translational and angular velocities, respectively. \vec{x}_c and $\vec{x} + \vec{c}_i \Delta t / 2$ are, respectively, the coordinates of the particle center of mass and the midboundary link. The momentum exchange information between fluid and solid is used to compute correctly the fluid force acting on a solid particle. For more detailed information, please refer to Refs. [47,57,58,71,74,75,85,86,92–94]. Note also that, at low to moderate Reynolds numbers, hydrodynamic actions on a particle are satisfactorily accounted for by the present numerical scheme provided that a resolution $R/h > 5$ is reached, with R being the particle radius [89].

In a 3D granular medium assembly, the pore space between the disks is interconnected, whereas in a 2D assembly, the particles are in contact with each other and consequently no fluid path exists throughout the densely packed particles. In order to overcome this difficulty, Boutt *et al.* [49,50] proposed to use a

hydraulic radius, R_h , in the fluid-solid two-way coupling. R_h is chosen smaller than the actual radius of a particle, R , which is adopted for a cylinder to give an equivalent drag force to a sphere [47,49,50,95]. The reduced value of the real particle size introduced by the hydraulic radius is used only during LBM computation to deal with the fluid-particle interaction but it has no effect on the particle interaction. For the DEM calculation, the real particle radius is employed in the computation. Hence, for generating artificially the fluid paths between the particles in two dimensional simulation, the hydraulic radius $R_h = 0.8R$ is adopted as in Refs. [47,49,50,95]. This value allows to keep a minimal gap between two particles larger than four lattice cells, in line with the requirements of the no-slip moving boundary [95]. With the different sets of parameters used in the present study, it also systematically preserves a resolution R_h/h larger than the minimum required limit of five [89].

The choice of the time-step parameters is also very important. There are two time steps used in the DEM-LBM framework, Δt for the fluid flow and Δt_D for the solid particles. In practice, the time step used in LBM is stated to be larger than that in DEM [47,52,57,58,85,86,90,94]. Therefore, one should perform a number N_{sub} of DEM computation steps during one LBM computation step. It is important to note that the hydrodynamic forces and torques remain constant during sub-cycling. With the DEM time step Δt_D^{sub} being imposed (see Sec. II B), the LBM time step is

$$\Delta t = N_{\text{sub}} \Delta t_D^{\text{sub}}. \quad (25)$$

The relaxation parameter τ of the LBM algorithm then depends on the time step Δt , the lattice spacing h , and the kinematic viscosity of fluid ν_f and reads

$$\tau = \frac{1}{2} + \frac{3\nu_f \Delta t}{h^2}. \quad (26)$$

D. Validation and benchmarking

Before presenting our numerical results on localized fluidization in a granular medium, we consider here the modeling ability of the LBM and the coupled LBM-DEM technique using immersed moving boundary method via two simple flow problems. To test the performance of the LBM-MRT model to simulate fluid flow, we applied it to the two-dimensional problem of the lid-driven cavity flow in a square cavity. Since no analytical solution is available for this problem, the simulation result will be compared with the work carried out by Ghia *et al.* [96]. Then, the performance of the hydrodynamic coupling will be demonstrated with the simulation of the 2D sedimentation of a circular cylinder in a channel. This flow has been used as a standard benchmark test in CFD and the drag coefficient of a circular cylinder as a function of the Reynolds number was investigated and positively compared with some previous experimental, analytical, and numerical results.

1. Two-dimensional lid-driven square cavity flow

The lid-driven square cavity flow has been used as a benchmarking problem for many numerical methods due to its simple geometry and complicated flow behaviors. The principal characteristics of the 2D square cavity flow are the emergence of the large primary vortex in the center and two

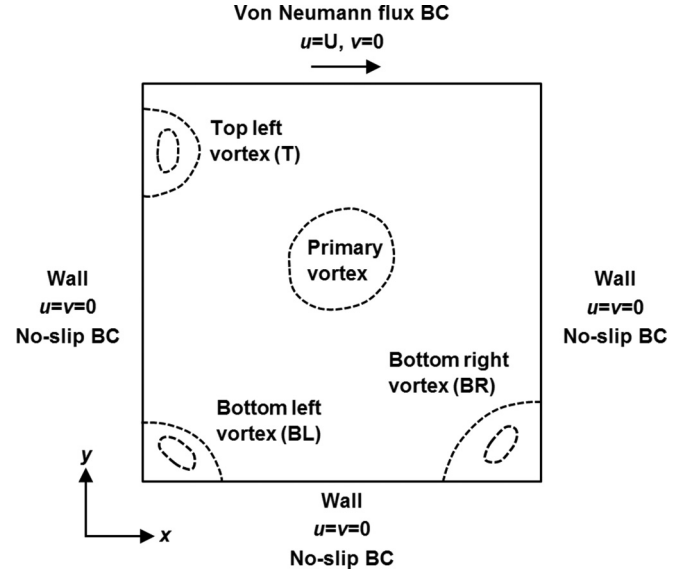


FIG. 4. Geometry and boundary conditions of the lid-driven square cavity flow.

secondary vortices in the lower corners. The locations of the centers of these vortices depend on the Reynolds number. The geometry and boundary conditions are shown in Fig. 4. The left, right, and bottom walls of the cavity are fixed ($u = v = 0$), and the top wall moves from left to right with a constant velocity ($u = U, v = 0$). The Reynolds number is defined as $Re = \frac{UL}{\nu_f}$ with L being the square length and ν_f being the fluid's viscosity.

The flow field is initialized by setting $\rho = 1$ and $\vec{u} = 0$. In simulations, the number of lattice nodes in each coordinate direction was taken as 129 or 257 for Reynolds numbers Re ranging from 100 to 10 000. In Figs. 5 and 6, the velocity profiles through the cavity center are plotted for different values of the Reynolds number and compared to the benchmark

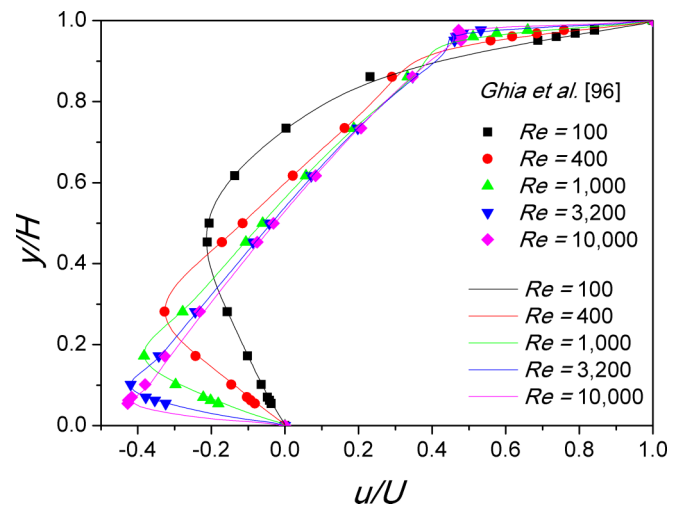


FIG. 5. Vertical profile at the center of the cavity of the horizontal velocity component u normalized by the top wall velocity U . Solid lines are our LBM-MRT solutions and symbols are benchmark solutions from [96] for different Reynolds number values.

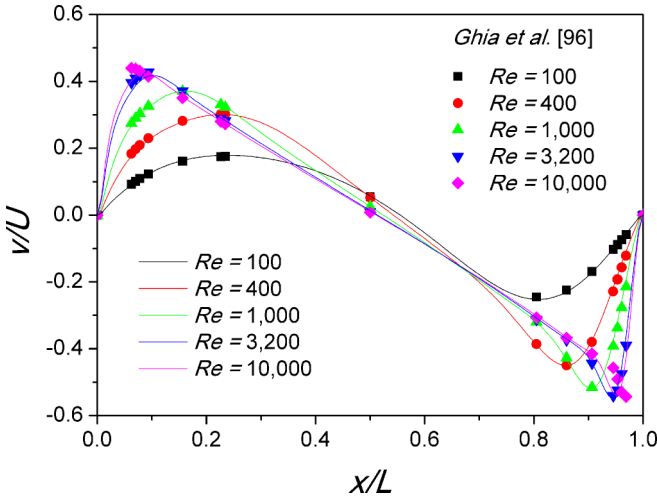


FIG. 6. Horizontal profiles at half the cavity height of the vertical velocity component v normalized by the top wall velocity U . Solid lines are our LBM-MRT solutions and symbols are benchmark solutions from [96] for different Reynolds number values.

solutions of Ref. [96]. One can see that our LBM calculations nicely agree with the benchmark solutions for all simulated values of Re . Additionally, the locations of the vortex cores (see Fig. 4) were also quantitatively determined for different values of Re with accurate prediction regarding previous calculations [96,97]. These results clearly show the general ability of LBM to simulate complex 2D fluid flows and supports validation of our own algorithm.

2. Two-dimensional sedimentation of a circular cylinder

The drag coefficient on a free-falling circular cylinder of diameter d within a fluid initially at rest was investigated at increasing values of Reynolds number Re , defined by $Re = \frac{ud}{\nu_f}$ with u being the relative velocity between the fluid and the cylinder and ν_f being the fluid's viscosity. The flow configuration is as follows: A disk of diameter $d = 1$ mm and density ρ_s falls vertically in the median plane of a rectangular box of width W and height L . Note that here the hydraulic radius is equal to the actual disk radius. In order to reduce the influence of inflow and outflow boundary conditions, the height of the channel was set to $L/d = 50$ while its width was $W/d = 8$. The no-slip boundary conditions were applied at the lateral as well as at the top and bottom walls of the channel. Interpolated bounce-back boundary conditions with a first-order interpolation were used for the implementation of momentum balance at the boundary between the fluid and the disk. The LBM domain was finely discretized with a lattice size step $h = D/40$ and the lattice speed was kept equal to $c = 1 \text{ m s}^{-1}$. The cylinder, initially released at a distance $l = 2L/3$ from the bottom of the box, quickly reaches a terminal velocity denoted U . The drag coefficient C_D of the disk can therefore be calculated as

$$C_D = \frac{2F_D}{\rho_f U^2 d} = \frac{\pi(\rho_s - \rho_f)gd}{2\rho_f U^2}, \quad (27)$$

where $\rho_f = 1000 \text{ kg m}^{-3}$ is the fluid density, $g = 9.81 \text{ m s}^{-2}$ is the gravity, and F_D is the hydrodynamic force acting on

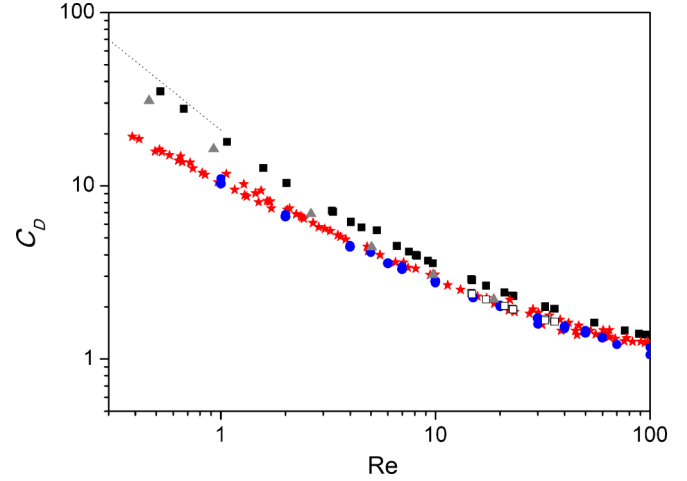


FIG. 7. Circular cylinder drag coefficient C_D as a function of Reynolds number: present results before (solid squares) and after (open squares) wall effect correction in the range $15 \leq Re \leq 40$ according to Ref. [103]; DEM-LBM computational results (gray triangles) by Owen and coauthors [51]; direct numerical calculations (blue circles) by Hamielec and Raal [98], Takami and Keller [99], Dennis and Chang [100], and Fornberg [101]; and experimental data by Tritton [102] (red diamonds); Faxén analytical expression for small Re values [104] (dotted line).

the cylinder (per unit length of the cylinder) that simply balances the buoyant weight in the stationary regime. By varying the particle density ρ_s and fluid kinematic viscosity ν_f , the Reynolds number Re calculated from the corresponding terminal velocities, i.e., $Re = \frac{Ud}{\nu_f}$, ranges between 0.5 and 100.

Figure 7 shows our computational results for the drag coefficient as a function of the Reynolds number. For comparison, several previous data in the equivalent problem of fluid flow past a circular cylinder are also plotted in the same graph: first, the results by Owen and coauthors [51] based on the DEM-LBM approach in rather similar conditions to our simulations; second, several semianalytical and direct numerical resolutions of Navier-Stokes equations by Hamielec and Raal [98], Takami and Keller [99], Dennis and Chang [100], and Fornberg [101]; and third, the experimental data obtained by Tritton [102] using quartz-fiber anemometers.

As can be seen from this graph, our results are quite close to the previous ones obtained by Owen and coauthors with similar DEM-LBM calculations. However, regarding the overall collapse of all the other values issued either from experiments or numerical resolutions of Navier-Stokes equations, the DEM-LBM computations substantially overestimate the drag coefficient, especially for small values of the Reynolds number. Considering that both the present study and the previous one by Owen and coauthors used no-slip conditions at the lateral walls, the discrepancy could arise from wall effects, especially in our case where the ratio of the particle diameter to the box or channel width is $d/W = 0.1$ compared to a ratio $d/W = 0.01$ in Owen's simulations.

Regarding the related situation of channel flow past a circular cylinder, Sen and coworkers [103] evaluated quantitatively for $15 \leq Re \leq 40$ the wall effect for different values of d/W and concluded that wall effect is insignificant as far as

TABLE I. Numerical samples used in the simulations with the number of particles, initial bed height H_0 and solid volume fraction Φ_0 .

Sample	Particle number	H_0 (mm)	Φ_0
S1	504	8.0	0.79
S2	1022	17.2	0.81
S3	1539	26.3	0.81
S4	2068	36.9	0.80
S5	2578	45.4	0.81
S6	3096	53.8	0.82
S7	3606	62.7	0.82
S8	4126	72.2	0.82
S9	4644	79.9	0.83
S10	5000	85.8	0.83

$d/W \leq 0.4$. Indeed, contrary to our data, those of Owen and coauthors do not reveal any influence of the boundary in this range of Reynolds numbers. From Sen's wall-effect estimate for $d/W = 0.11$, a value rather close to our case where $d/W = 0.125$, we can infer the unbounded drag coefficients for our data. As can be seen in Fig. 7, the corrected values collapse nicely on the general curve. An analytical calculation accounting for wall-effect correction at very small Reynolds number (i.e., Stokes flow) has also been proposed long ago by Faxén as a function of d/W [104]. As shown in Fig. 7, a satisfactory agreement is consistently obtained with our data when plotting Faxén relation for $d/W = 0.125$ in the range $Re \leq 1$ (in dotted line).

III. SIMULATION OF LOCALIZED FLUIDIZATION

A. Configuration

Based on the coupled LBM-DEM approach described in the previous section, two-dimensional numerical simulations were carried out to study the action of a localized fluid injection at the bottom of an assembly of grains. The particle diameters were uniformly distributed from $d_{\min} = 0.8d$ to $d_{\max} = 1.2d$, where d is the mean particle diameter. All the calculations were carried out with $d = 2$ mm, except in one case where the diameter was doubled.

The fluid domain was divided into a square lattice of dimensions $L_x \times L_y = 1385 \times 801$ with an elementary spacing $h = 0.16$ mm or, equivalently, a spatial resolution $d_{\min}/h = 10$. Hence, the physical dimensions of the domain were $L \approx 222$ mm in length and $H \approx 160$ mm in height. Ten different granular beds, denoted from S1 to S10, were created by the following procedure. The particles were initially placed at the nodes of a regular grid within a rectangular box and then released under the action of gravity until complete deposition. As specified in Table I, the number of particles was increased by one order of magnitude, from 504 to 5000, giving rise to initial bed heights ranging from $H_0 = 8.0$ mm for S1 to $H_0 = 85.8$ mm for S10. All the initial assemblies have a rather similar solid volume fraction $\Phi_0 = 0.82 \pm 0.01$, except samples S1 and S4, which were slightly less dense. Most of the results presented in the following have been obtained for the

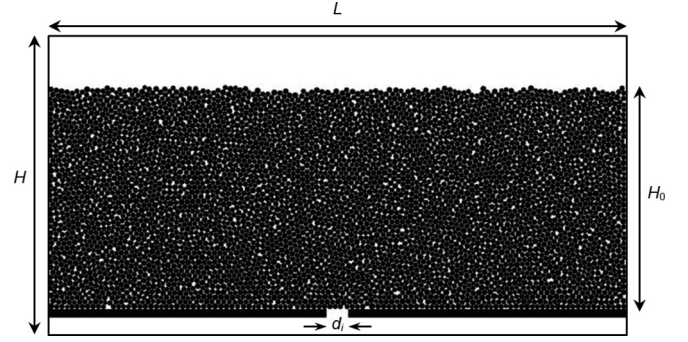


FIG. 8. Definition of the geometry and integration domain under study.

two samples S6 and S10 with initial bed heights $H_0 = 53.8$ mm and $H_0 = 85.8$ mm, respectively.

The whole domain is saturated by a fluid and the corresponding boundary conditions were no-flow and no-slip on the left and right frontiers, considered as solid walls, while periodic boundary conditions were applied at the top and bottom frontiers. In its initial configuration, the granular layer rested on an horizontal wall with, at its center, an aperture of length d_i that was impenetrable for the grains but perfectly permeable to the fluid. Most of the calculations were carried out for a small injection diameter $d_i = 50h = 8$ mm, or equivalently $d_i/L \approx 0.036$, except a few of them for which a systematic study of the influence of d_i was undertaken (see Sec. IV C). In all cases, a constant velocity U was imposed at the injection hole. A sketch of the numerical configuration is shown in Fig. 8.

In addition to h , the other free LBM parameter was the lattice speed whose value was taken equal to $c = 10$ m s⁻¹. Thus, the corresponding time step was $\Delta t = h/c = 1.6 \times 10^{-5}$ s. The substeps of integration were kept equal to $N_{\text{sub}} = 2$, meaning that the DEM time step was twice the LBM one. Finally, the following parameters were chosen for the DEM modeling of the particles: normal contact stiffness $k_n = 10^5$ N m⁻¹, coefficient of regularization $K_t = k_n N_{\text{sub}} \Delta t$, friction coefficient $\mu = 0.3$ (both between two particles and between a particle and a wall), and damping coefficient γ_n deduced from Eq. (21) so that a realistic coefficient of restitution $e = 0.2$ is obtained.

B. Parameters under study

To reach a fluidized state, the drag forces induced by the interstitial flow must overcome the interparticle forces within the granular assembly. In the studied condition of purely frictional interactions between solid particles, the internal granular stress is solely related to the buoyant weight of the system. Consequently, the physical parameters of the problem are the density of the solid particles ρ_g , the mean particle diameter d , the fluid kinematic viscosity ν_f , and the fluid density ρ_f , the latter being always equal to $\rho_f = 10^3$ kg m⁻³. The geometry parameters are the initial bed's height H_0 , the bed's width L , and the injection hole diameter d_i .

In what follows, several parametric studies of the granular bed subjected to localized fluidization are presented focusing successively on the final steady-state regimes reached by the system, particularly with a view to draw a phase diagram and

TABLE II. Table of parameter sets used in our simulations.

Set	v_f ($\text{m}^2 \text{s}^{-1}$)	ρ_g (kg m^{-3})	g (m s^{-2})	d (mm)
A	5×10^{-5}	2500	9.81	2.0
B	1×10^{-5}	2500	9.81	2.0
C	5×10^{-5}	2500	1.0	2.0
D	1×10^{-5}	1500	9.81	2.0
E	5×10^{-5}	1500	9.81	2.0
F	5×10^{-5}	2500	1.0	2.0
G	5×10^{-6}	2500	9.81	2.0
H	5×10^{-6}	1500	9.81	2.0
I	2×10^{-6}	2500	9.81	2.0
J	2×10^{-6}	1500	9.81	2.0
K	5×10^{-5}	2500	9.81	4.0

on the analysis of hysteresis effects during velocity increase-decrease procedures (see Sec. IV A), on the previous transient regime on the route to chimney fluidization (see Sec. IV B), and finally on the influence of the injection width on the previous observations (see Sec. IV C).

As described in Table II, eleven different sets of the physical parameters v_f , ρ_g , g , and d were used in the present study.

For each configuration based on a parameters set with a given sample, several simulations (typically from 10 to 20) were carried out where the injection velocity U was progressively increased and used as a control parameter of fluidization. For computational time requirements and given the large number of individual simulations (more than 900), the physical time simulated during each calculation was restricted to a total duration of 10 s (except when specifically mentioned).

IV. NUMERICAL RESULTS

A. Stationary states and hysteresis

The following study of stationary states and hysteresis effect of localized fluidization was implemented for a unique value of injection width d_i , namely $d_i/h = 50$, or equivalently $d_i/L = 0.036$. Typical results obtained for a given choice of physical and geometry parameters are shown in Fig. 9 when the injection velocity is progressively increased. This figure, reporting the case of sample S10 and parameters set I, provides examples for each of the three different types of final states that can be observed at the end of the 10-s duration of the simulations, *a priori* assuming that those are almost stationary.

As observed in Fig. 9(a), a low injection velocity does not modify the bed's structure, or only very marginally through a slight overall dilation of the grain packing. Then, the sample remains static and behaves simply as a rigid porous medium. Conversely, a stronger injection at a significantly higher velocity induces fluidization of the grains at the flow exit that progressively develops upward to the top of the granular bed and reaches eventually a stationary state of fluidized chimney as illustrated in Fig. 9(c). The transient regime will be closely examined in Sec. IV B. In the final stationary state, the ascending flux of fluidized grains along the chimney is steadily balanced by lateral downward avalanches of grains within the dense part of the sample. Between those two steady

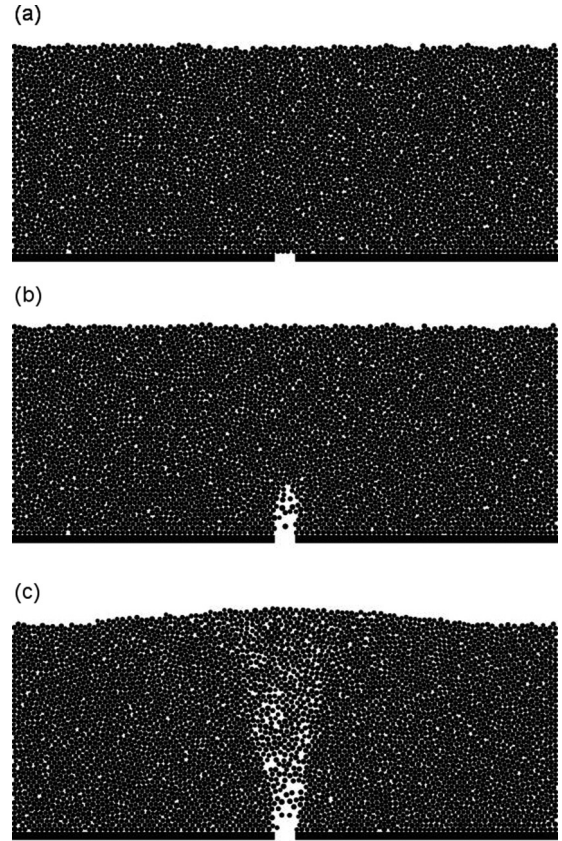


FIG. 9. Typical steady states observed for increasing value of the injection velocity U with sample S10 ($H_0 = 85.8$ mm) and parameter set I: (a) Static bed for $U = 0.10$ m s^{-1} ; (b) fluidized cavity for $U = 0.20$ m s^{-1} ; and (c) fluidized chimney for $U = 0.30$ m s^{-1} .

states, a third regime can be observed for intermediate injection velocities, where the fluidized domain does not expand until the top of the sample but remains restricted to a cavity. This fluidized cavity is characterized by turbulent and chaotic motions of grains inside the cavity as well as some fluctuations of the height of the fluidized zone. In some cases, essentially no fluidized cavity can be noted and the system apparently jumps directly from a static bed to a stationary fluidized chimney.

Regarding this general phenomenology, two critical injection velocities, denoted respectively U_{cav} and U_{ch} , must be used to define the frontiers between the three stationary regimes:

- (1) *static* regime when $U < U_{\text{cav}}$;
- (2) *fluidized cavity* regime when $U_{\text{cav}} < U < U_{\text{ch}}$; and
- (3) *fluidized chimney* regime when $U > U_{\text{ch}}$.

It must be emphasized here that the distinction between a fluidized cavity and a fluidized chimney is far from obvious, especially in the present study where the duration of the simulations is restricted to 10 s. Indeed, a fluidized chimney whose transient evolution exceeds this time limitation will be considered as a fluidized cavity. As a consequence, the estimates of U_{cav} and U_{ch} are somehow arbitrary whereas a more relevant and unbiased way of defining a critical chimney velocity will be presented in the next section dedicated to the transient.

However, on the basis of these definitions, phase diagrams can be plotted for different samples (or equivalently bed height

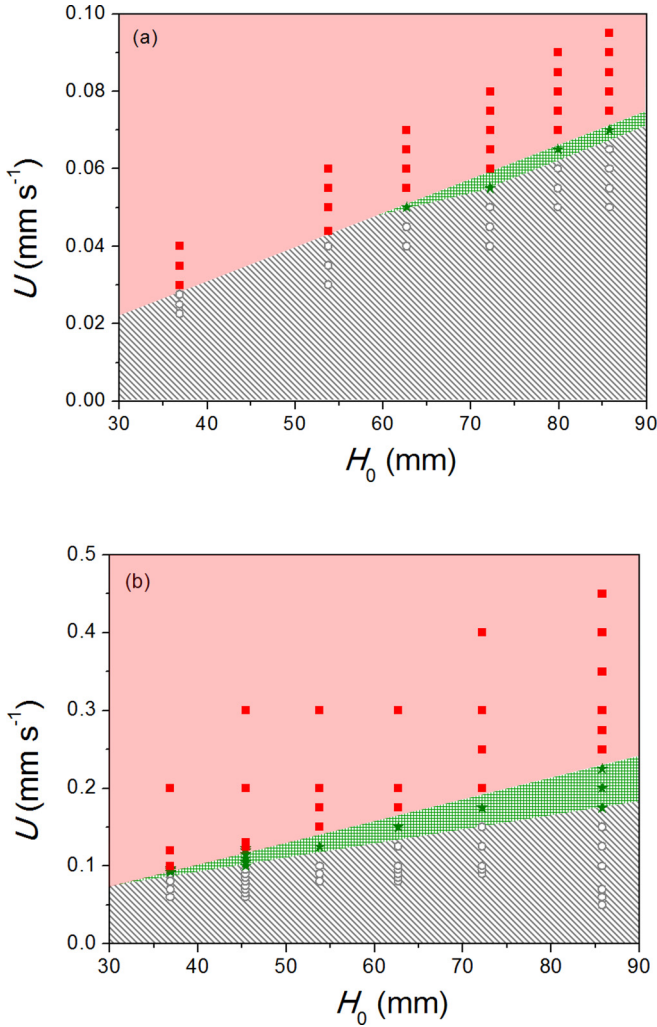


FIG. 10. Phase diagrams discriminating the different steady states, namely *static* (circles and hatched gray area), *fluidized cavity* (stars and grid green area), and *fluidized chimney* (squares and plain red area), obtained with sample S10 for (a) parameters set A and (b) parameters set I.

H_0 in the present study) and parameter sets A and I, as illustrated in Fig. 10. Each point in those diagrams corresponds to an individual 10-s simulation for a given set of physical and geometrical parameters.

Two remarks are essential in this respect. First, the boundaries of the different phase domains are consistent with a linear dependence with the bed height H_0 . This result will be confirmed in the following section regarding chimney threshold. Second, the fluidized cavity regime is only observed for the parameter set I and virtually not for the parameters set A whereas the only difference here is the fluid viscosity: $\nu_f = 5 \times 10^{-5} \text{ m}^2 \text{ s}^{-1}$ for set A and $\nu_f = 2 \times 10^{-6} \text{ m}^2 \text{ s}^{-1}$ for set I. This influence of the fluid viscosity will be discussed later in Sec. V C. It should also be noted that the range of injection velocity where the *fluidized cavity* regime is observed tends to extend slightly with an increase in the bed height as shown in Fig. 10(a) and is consistent with previous experimental evidences [23,37,38].

Similar steady states are obtained when one does not use anymore individual simulations at constant injection velocity but a complete sequence with incremental progression of the injection velocity U by successive stages of constant values (for which the 10-s duration is kept). Of great interest is then the behavior of the system when the injection velocity is decreased back by a reverse sequence. Indeed, previous experiments [37,38] have reported that the fluidized cavity regime is then sustained until values of U are drastically smaller than U_{cav} . This tremendous hysteresis effect was interpreted in terms of the creation of arches within the newly formed upper grain layer of the sample when the fluidized chimney closes back and then as the fluidized cavity progressively diminishes [38].

The same sequences of increase and then decrease of the injection velocity were simulated with sample S10 and parameters set A and I. A hysteresis effect was observed, but to a quite much lesser extent as is shown in Fig. 11, where the ratio of the height of the fluidized area H_f (see Sec. IV B for quantitative definition) to the initial sample height H_0 is plotted against the injection velocity U normalized by the chimney threshold velocity U_{ch} .

As will be further discussed in depth in Sec. V B, the reason for this discrepancy between experimental and numerical results could be related to the difference in terms of space dimensionality since the experiments are intrinsically 3D whereas our simulations are solely two dimensional. However, similarly to previous experimental results [37,38], a fourth stationary regime, called *potential fluidized cavity*, can be observed in the velocity domain where the sample remained static during the increasing phase but was still locally fluidized during the decreasing phase, even if, as already mentioned, this domain is quite limited compared to experimental findings. It is to be noted also that this new regime exists even when the *fluidized cavity* regime has not, or evanescently, been observed during the prior increasing velocity phase, as is the case for parameter set A in Fig. 11(a).

Despite the fact that the hysteresis effect appears to be far much less important in our 2D simulations, its origin should be of the same nature as suggested from the experiments and mentioned before: Arches are continuously formed during cessation of fluidization on top of the fluidized area, allowing the increasing burden to be partially transmitted to the lateral zones of the sample. As shown in Fig. 12, the normal contact forces distribution within the sample in the *potential fluidized cavity* regime is substantially consistent with this explanation. Indeed, a comparison between the forces distribution observed before (black arrow in Fig. 11) and after (red arrow in Fig. 11) complete chimney fluidization seems to reveal the appearance in the postfluidized sample of a slightly stronger upper arch above the cavity together with several inclined lateral force chains.

B. Transient regime and chimney threshold

Following the previous study on steady states in Sec. IV A, the influence of the initial height H_0 on the transient regime was studied for samples 5 to 10 with the parameter set A. Then, a first parametric study was carried out using sample S10 with all the different parameters sets given in Table II, enabling some of the physical parameters to be significantly varied, namely

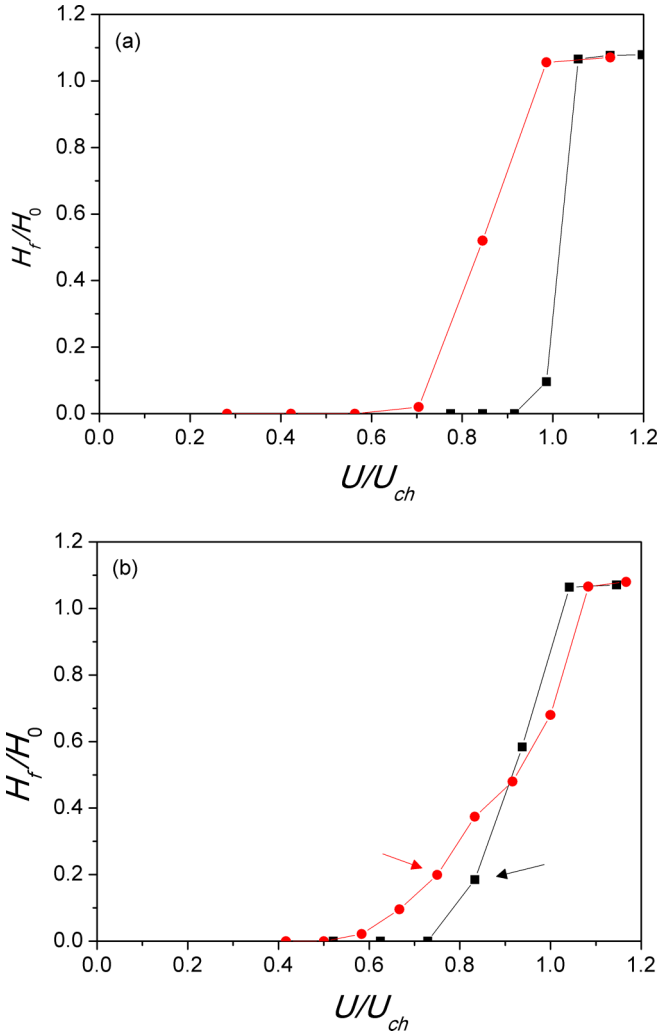


FIG. 11. Ratio of the height H_f of the fluidized zone to the initial sample height H_0 vs the dimensionless injection velocity U/U_{ch} obtained at the end of successive stages of injection velocity U during prior increasing velocity sequence (black squares) and subsequent decreasing velocity sequence (red circles) with sample S10 ($H_0 = 85.8$ mm): (a) parameters set A, critical chimney velocity $U_{ch} = 0.071$ m s $^{-1}$, velocity increments 0.005 m s $^{-1}$ (increasing sequence), and 0.010 m s $^{-1}$ (decreasing sequence); (b) parameters set I, critical chimney velocity $U_{ch} = 0.24$ m s $^{-1}$, velocity increments 0.025 m s $^{-1}$ (increasing sequence), and 0.020 m s $^{-1}$ (decreasing sequence). The red and black arrows denote the samples for which the normal contact forces network is later plotted in Fig. 12.

ν_f , ρ_g , d and the gravitational acceleration g . Lastly, a second parametric study was based on a smaller bed, namely S6 with $H_0 = 53.8$ mm, using only the parameter sets A, D, F, G, and I. Here, the injection width was kept fixed for all simulations: $d_i = 8$ mm. A few previous results of this parametric study of the transient regime to fluidized chimney were presented elsewhere by the authors [105]. A lot of more detail, analysis, and discussion will be found in the following.

Our quantitative investigation of the transient regime was carried out as follows. First, for each set of parameters, several simulations were implemented with increasing values of the injection velocity U . Once the velocity was high enough for

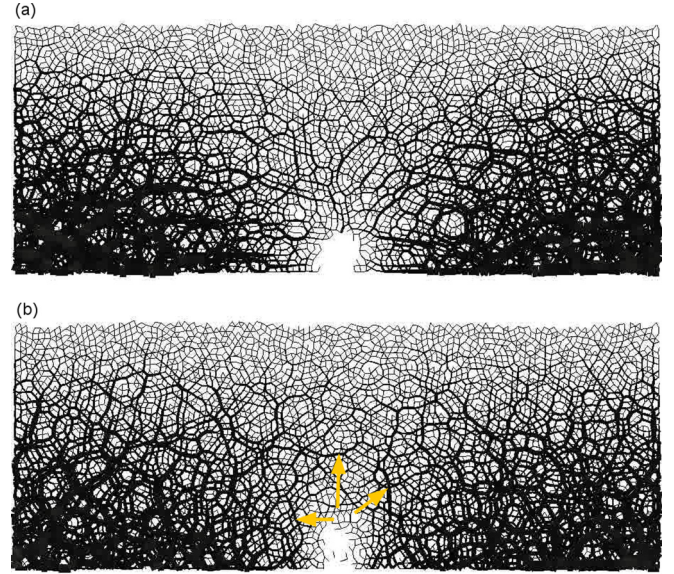


FIG. 12. Typical network of normal contact forces within sample S10 with parameter set I during both (a) increasing and (b) decreasing injection velocity sequences, before and after chimney fluidization as identified in Fig. 11 by black and red arrows, respectively. In these graphs, the thickness of each segment connecting the centers of two grains in contact is proportional to the corresponding value of the normal contact force. The orange arrows in panel (b) denote the location of stronger force chains, presumably able to create an arch.

a fluidized chimney to be obtained by the end of the total 10-s duration of the computation, a space-time diagram was constructed as in Fig. 13. For this, we used the pixel values given by the LBM calculation in between 0 (pixel inside a fluid cell) and 1 (pixel inside a solid cell). These values were averaged to evaluate the mean void fraction on each horizontal line inside a region of interest (ROI), a rectangular area of width equal to d_i , located just above the injection hole and slightly higher than the initial bed height H_0 [see Fig. 13(a)]. Then, the space-time diagram was constructed by arranging all the mean void fraction profiles of the ROI calculated at successive times [see Fig. 13(b)]. At last, a manual detection allowed us to obtain the evolution of the fluidized height H_f above injection as a function of time and to define accurately the characteristic transient time t_0 needed for the fluidized area to reach the initial bed height H_0 , i.e., $H_f(t = t_0) = H_0$ [see Fig. 13(c)].

As can be seen in Fig. 14, the time t_0 systematically tends to diverge as the injection velocity U decreases and a critical value U_c can be defined by adjustment with the following expression:

$$t_0(U) = t_c \left(\frac{U}{U_c} - 1 \right)^{-\alpha}, \quad (28)$$

where t_c is given by $t_c = t_0(U = 2U_c)$ and the exponent α varies almost always between 0.45 and 0.75 (see inset in Fig. 14).

Note that due to the almost unavoidable restriction of the total duration of the simulations to 10 s, it is not possible to come very close to the divergence asymptote and to achieve therefore a better precision for U_c , t_c , and α . However, while a significant sensitivity to fitting procedure is observed for the exponent α , the values obtained for U_c and t_c are robust and

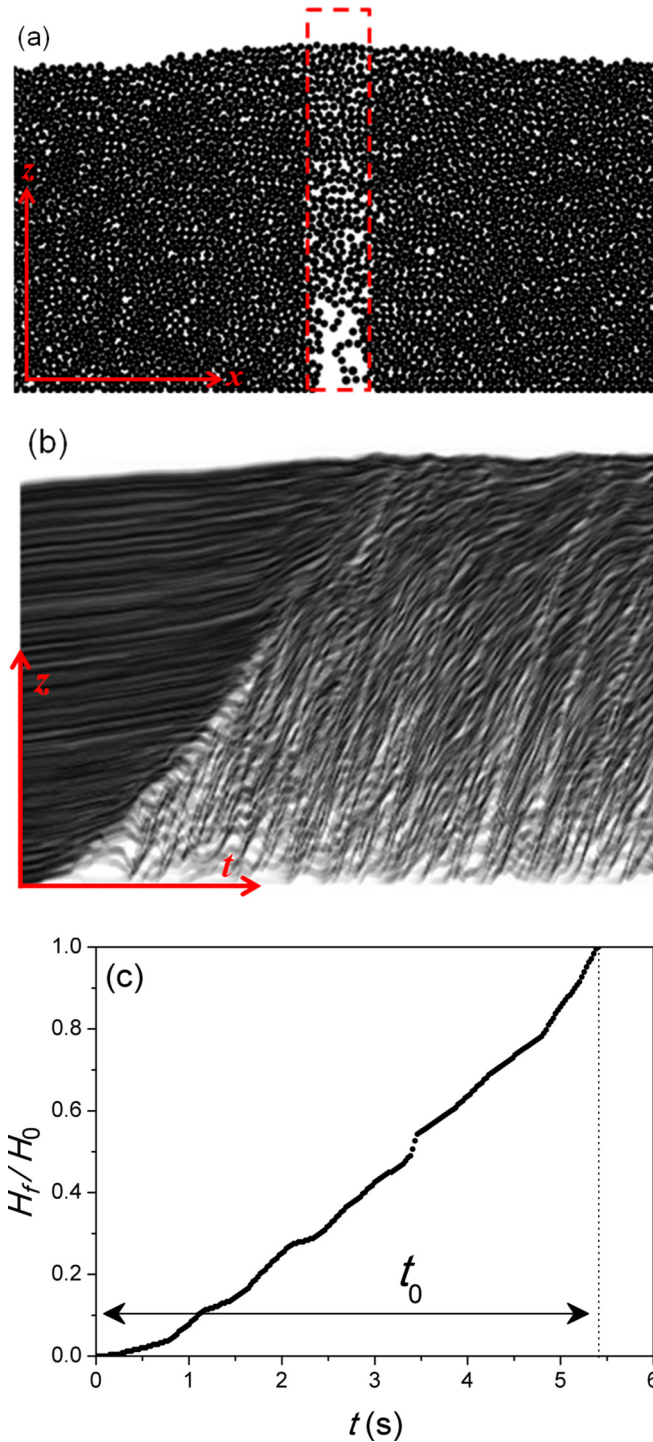


FIG. 13. (a) Definition of the region of interest (ROI) above the injection hole. (b) Space-time diagram. (c) Height of the fluidized zone H_f vs time after manual detection and practical definition of a characteristic transient time t_0 by $H_f(t = t_0) = H_0$.

reliable. For instance, when testing the same fitting procedure with a fixed exponent $\alpha = 0.6$, U_c and t_c were only marginally modified, by less than 5% in most cases.

For a given set of physical parameters, the critical velocity U_c is observed to increase almost proportionally with H_0 as shown in Fig. 15(a) for the parameter set A. This result is

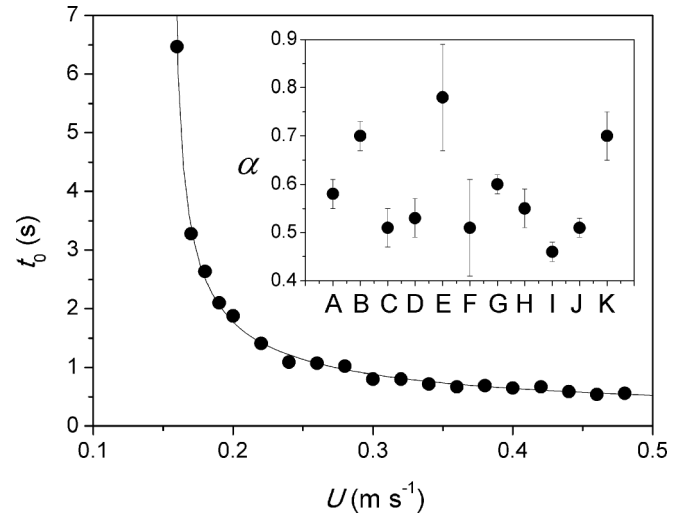


FIG. 14. Typical divergence of the transient time t_0 as a function of the injection velocity U . The data presented here correspond to the parameters set G with sample S10. The dotted line is the divergent power-law expression (28) with $U_c = 0.1547 \text{ m s}^{-1}$, $t_c = 0.85 \text{ s}$, and $\alpha = 0.60$. Inset: values of α with error bars obtained for the 11 parameter sets from A to K when α is kept as a free parameter in the fitting form. The mean value is $\bar{\alpha} = 0.58 \pm 0.10$.

consistent with the first experiments by Zoueshtiagh [34] and the subsequent ones by Philippe and Badiane [38], where a linear relationship was observed. Note that it has been shown recently, both experimentally and theoretically, that the critical velocity is only linear for small bed heights and it gradually saturates for thicker granular layers up to the critical value obtained for homogeneous fluidization [37]. Of interest is also the behavior of the characteristic transient time t_c with the bed height H_0 . Compared to U_c , t_c is not proportional to H_0 but a linear behavior is consistent with the data as plotted in Fig. 15(b).

To gain a better insight into the physical origin of both the critical injection velocity U_c and the characteristic transient time t_c , a systematic variation of v_f , ρ_g , d , and g was investigated using all the different parameter sets of Table II with the same particle assembly, namely sample S10 having an initial height equal to $H_0 = 83.8 \text{ mm}$. The results can be nicely analyzed in terms of dimensionless groups. To this end, U_c and t_c are beneficially replaced by a critical Reynolds number Re_c and a dimensionless transient time τ_c defined as follows:

$$\text{Re}_c = \frac{U_c d}{v_f}, \quad (29)$$

$$\tau_c = \frac{t_c v_f}{d^2}. \quad (30)$$

In addition, using v_f , d , and the reduced gravity defined by $g^* = (\frac{\rho_g}{\rho_f} - 1)g$ as the only physical parameters, a relevant dimensionless group in the context of fluidization is the Archimedes number, given by

$$\text{Ar} = \frac{g^* d^3}{v_f^2}. \quad (31)$$

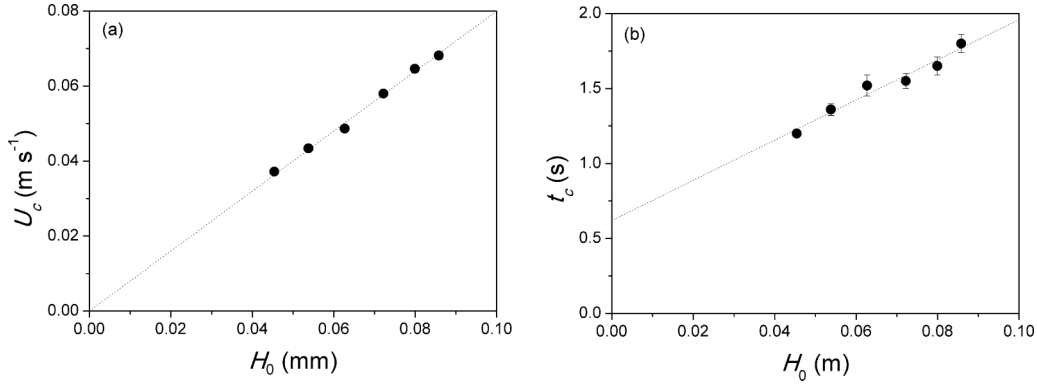


FIG. 15. The critical injection velocity U_c (a) and typical transient time t_c (b) obtained by adjustment of the divergence law (28) as a function of the initial bed height H_0 . The dotted line in panel (a) stands for the proportionality relation $U_c = AH_0$ with $A = 0.80 \text{ s}^{-1}$ whereas the dotted line in panel (b) is a linear relation given by $t_c = a + bH_0$ with $a = 0.62 \text{ s}$ and $b = 13.4 \text{ s m}^{-1}$.

Then, although Re_c and τ_c vary over three orders of magnitude according to our 11 different choices in physical parameters, all the data gather quite nicely when both Re_c and τ_c are plotted versus Ar , as shown in Fig. 16.

Accordingly to the previous dimensional analysis, it can be reasonably concluded that Re_c and τ_c are simply functions of the Archimedes number Ar . As can be seen in Fig. 16, the two related functions seem to be satisfactorily approximated by the following power law relations:

$$\text{Re}_c \propto \text{Ar}^{3/4} \quad (32)$$

and

$$\tau_c \propto \text{Ar}^{-3/4}, \quad (33)$$

with the two proportionality coefficients being 0.103 ± 0.003 and 543 ± 35 , respectively.

These empirical expressions suggest therefore the following dimensional scalings for U_c and t_c : $U_c \propto g_*^{3/4} d^{5/4} v_f^{-1/2}$ and $t_c \propto g_*^{-3/4} d^{-1/4} v_f^{1/2}$. Moreover, the critical velocity U_c and the typical transient time t_c appear consequently to be very simply related as

$$t_c \propto \frac{d}{U_c}, \quad (34)$$

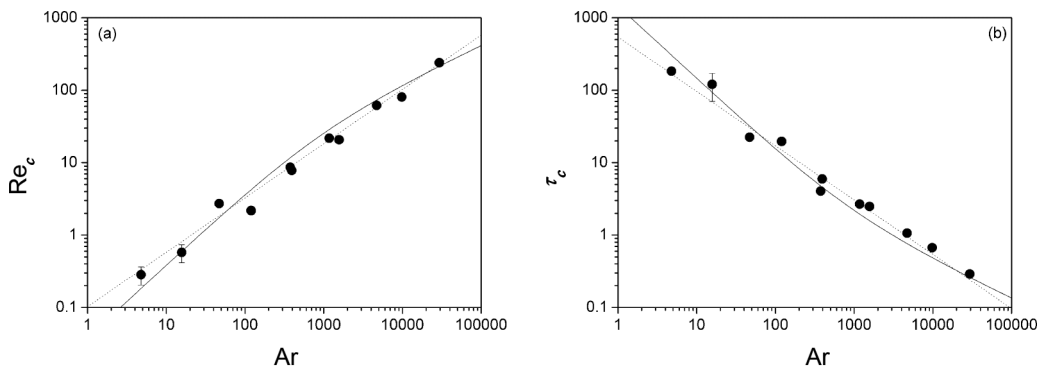


FIG. 16. Plot of (a) the critical Reynolds number Re_c and (b) the dimensionless transient time τ_c as a function of the Archimedes number Ar . The dotted lines correspond respectively to $\text{Re}_c = 0.103\text{Ar}^{3/4}$ and $\tau_c = 543\text{Ar}^{-3/4}$ while the solid lines are deduced from the Ergun relation $\text{Ar} = c_1\text{Re}_c + c_2\text{Re}_c^2$ (with $c_1 = 26$ and $c_2 = 0.52$) by additional use of Eq. (34) regarding τ_c .

where the proportionality coefficient is $\simeq 56 \pm 20$. As plotted in Fig. 17, this relation is almost correct but with less accuracy compared to previous scaling curves in Fig. 16.

Back to previous results about Re_c and τ_c in Fig. 16, the relation between Re_c , the critical Reynolds number for localized fluidization, and the Archimedes number Ar was theoretically and experimentally investigated and, for small enough values of Re_c , typically $\text{Re}_c < 10$ [106], a linear dependence was found due to the Darcy law for the fluid flow through the granular bed [37]. However, for higher Reynolds numbers, as is the case in the present study, the Darcy relation is no more valid and, for higher efficiency, can be substituted by the Ergun law, that proposes the following empirical relation between Archimedes number Ar and critical Reynolds number Re_c [106]:

$$\text{Ar} = \frac{150\Phi_0^2}{(1-\Phi_0)^3}\text{Re}_c + \frac{1.75\Phi_0}{(1-\Phi_0)^3}\text{Re}_c^2 \quad (35)$$

with Φ_0 the initial solid volume fraction of the granular bed.

The benefit of the use of the Ergun law compared to the Darcy law was only marginally evidenced in previous experiments [37,38], where the critical Reynolds number did not exceed 10. But here, Reynolds numbers up to 240 are obtained and the deviation from a simple linear dependency between Re_c and Ar can be more consistently understood by use of an Ergun-type relation than with our previous empirical

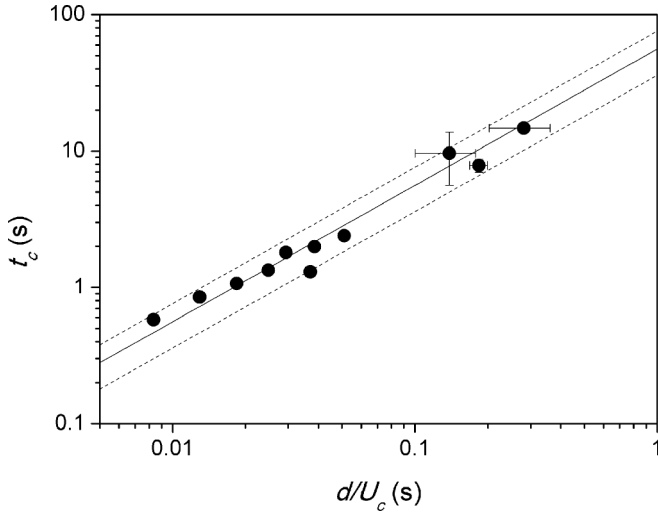


FIG. 17. Characteristic transient time T_0 vs d/U_c with U_c the critical injection velocity. The solid line represents a proportionality coefficient equal to 56 and the two dashed lines account for an uncertainty ± 20 .

power law $Re_c \propto Ar^{3/4}$. The Ergun expression in Eq. (35) cannot be directly duplicated to our numerical results since the geometry is 2D in the simulations. However, the general structure, composed of both linear and quadratic contributions, rather satisfactorily accounts for the data previously presented in Fig. 16(a). As also shown in Fig. 16(b), the same conclusion holds for τ_c when Eq. (34) is additionally used to deduce τ_c from Re_c .

Almost similar results are observed for the data obtained from the second parametric study with sample S6 using parameter sets A, D, F, G, and I. The scaling laws given by Eqs. (32), (33), and (34) remain fully valid, except the proportionality coefficients that are systematically smaller compared to the ones found for sample S10. One recovers here the influence of the initial bed's height H_0 as evidenced at the beginning of the present section. Note also that a larger dispersion is observed for the exponent α of the divergent power law proposed for t_0 versus U [see Eq. (28)].

To complete this analysis of transient regime to fluidized chimney, one can go beyond the two parameters U_c and t_c that

determine a critical threshold and a typical duration as we have just seen, and pay closer attention to the kinetics of localized fluidization. To this end, of probably greater interest than the transient time t_0 defined previously is the mean growth rate V_0 that reads

$$V_0 = \frac{H_0}{t_0}. \quad (36)$$

The quantity V_0 provides an average growth rate of the fluidized zone that is generated at injection and expands upward with time more or less rapidly.

As can be seen in Fig. 18(a), where all the data with sample S10 and parameters sets from A to K have been collected, V_0 can reach values as high as 0.2 m s^{-1} for the largest injection velocities U explored in the present study. V_0 gradually decreases for smaller values of U and finally tends to zero at the critical velocity U_c . According to the definition of V_0 [see Eq. (36)], the evolution of V_0 with U has an inverse power law relation than the one obtained for t_0 and given in Eq. (28). Therefore, it is natural to normalize the growth rate using the critical velocity U_c in order to collapse the data by plotting them against U/U_c (or equivalently Re/Re_c). More precisely, regarding the power law relation in Eq. (28), V_0/U_c is preferentially plotted against $U/U_c - 1$ as shown in Fig. 18(b). Then, considering the fact that for different parameter sets the exponent α is dispersed around an average value close to $3/5$ (see inset to Fig. 14), all the data of Fig. 18(a) collapse rather convincingly around a unique curve as follows:

$$\frac{V_0}{U_c} \propto \left(\frac{U}{U_c} - 1 \right)^{3/5}. \quad (37)$$

In the first parametric study carried out with sample S10, the proportionality coefficient of Eq. (37) is around 0.75. As can be seen in Fig. 19, when plotting those data together with those obtained for sample S6 using parameter sets A, D, F, G, and I, the same collapse of the data is observed, compatible here again with Eq. (37) but with a slightly larger proportionality coefficient approximately equal to 0.95. This is a reminiscence of the influence of the initial bed's height H_0 that is not completely accounted for by the previous scaling and suggests a more complex dependence with respect to the geometry of the sample, in the line with the recent theoretical proposal by

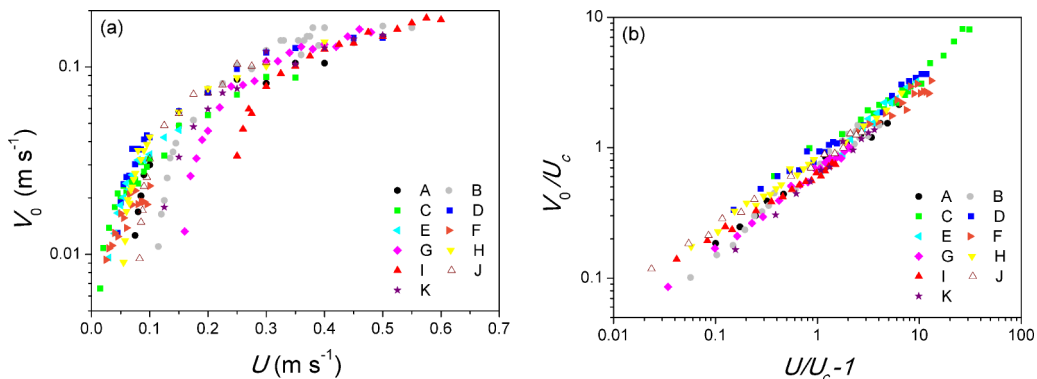


FIG. 18. (a) Mean fluidized cavity growth rate V_0 vs injection velocity U for all parameter sets from A to K with sample S10. (b) Dimensionless growth rate V_0/U_c vs $U/U_c - 1$. The solid line corresponds to Eq. (37) with a proportionality coefficient of 0.75.

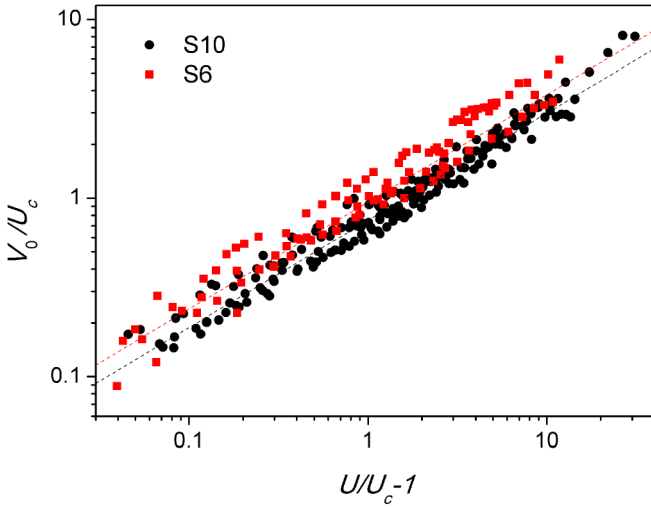


FIG. 19. Dimensionless growth rate V_0/U_c vs $U/U_c - 1$ for sample S10 with all parameters sets from A to K (black circles) and for sample S6 with parameters sets A, D, F, G, and I (red squares). The dotted lines correspond to Eq. (37) with proportionality coefficients of 0.75 (black line) and 0.95 (red line), respectively.

Mena and coauthors [37] already mentioned previously, but that would need here to be adapted to the present 2D modeling.

C. Influence of the injection size

In all numerical results so far analyzed, the configurations under study were restricted to a small injection size d_i compared to the total length L of the granular sample: $d_i/L \approx 0.036$. In this section, the influence of the injection size d_i is specifically investigated, from $d_i/L \approx 0.018$ to $d_i/L = 1$, with the two samples S6 and S10, and for both parameter sets A and I that differ only in terms of kinematic viscosity: $\nu_f = 5 \times 10^{-5} \text{ m}^2 \text{ s}^{-1}$ for A and $\nu_f = 2 \times 10^{-6} \text{ m}^2 \text{ s}^{-1}$ for I (see Table II). More precisely, for each of the four different options in sample and parameters set, a systematic variation of d_i was analyzed by use of the following injection sizes: $d_i/h = 25, 50, 100, 150, 200, 300, 400, 500, 600, 800, 1000, 1200$, and 1385. Note that the calculations with sample S6

were not carried out for $d_i/h = 150, 400, 600, 800$, and 1200. For all these configurations, simulations were successively run with increasing injection velocity U . Then, exactly the same fitting procedure, based on Eq. (28) and described previously in Sec. IV B, was used to determine the critical velocity U_c , the typical transient time t_c , and the exponent α . Most of these simulations were run with significantly less individual calculations, each of them related to a given injection velocity U . As a consequence, the two fitting parameters t_c and α are not always easily or accurately extracted from the adjustment. From Fig. 20, we may plausibly assume that the characteristic transient time t_c remains more or less constant with substantial statistical variations from one value of d_i to another. The same holds also for exponent α , except for injection sizes that tend to the total length L and for which α seems to notably decrease, typically from 0.6 to 0.2.

On the contrary, the critical velocity U_c is much less versatile and can be quite accurately estimated. Figure 21(a) shows for sample S10 that, as expected, U_c rapidly decreases when the injection size d_i is increased, until a plateau is reached when $d_i \rightarrow L$, i.e., when one recovers the uniform and homogeneous fluidization situation, with a critical velocity U_c^h (see, for instance, Ref. [37]).

Regarding the relative gap between the actual critical velocity U_c at a given injection size d_i and the asymptotic homogeneous fluidization velocity U_c^h , the following empirical relation provides a reasonable agreement as shown in Fig. 21(b):

$$\frac{U_c - U_c^h}{U_c^h} \propto \left(\frac{L}{d_i} - 1 \right)^\beta, \quad (38)$$

where the exponent β remains rather close to 1, namely $\beta \approx 0.85$ and $\beta \approx 1.2$ for parameter sets A and T. Proportionality coefficients are approximately 0.018 and 0.060, respectively.

It is to be noted in Fig. 21 that, for a given injection size d_i , the data of U_c related to parameter set I differ from U_c^h in a much larger extent than for parameter set A. Very similar results are obtained for sample S6, with exactly the same discrepancy between parameter sets A and I (exponent $\beta \approx 1.1$ and $\beta \approx 1.3$, and proportionality coefficients around 0.007 and 0.030 for parameter sets A and I, respectively). As already

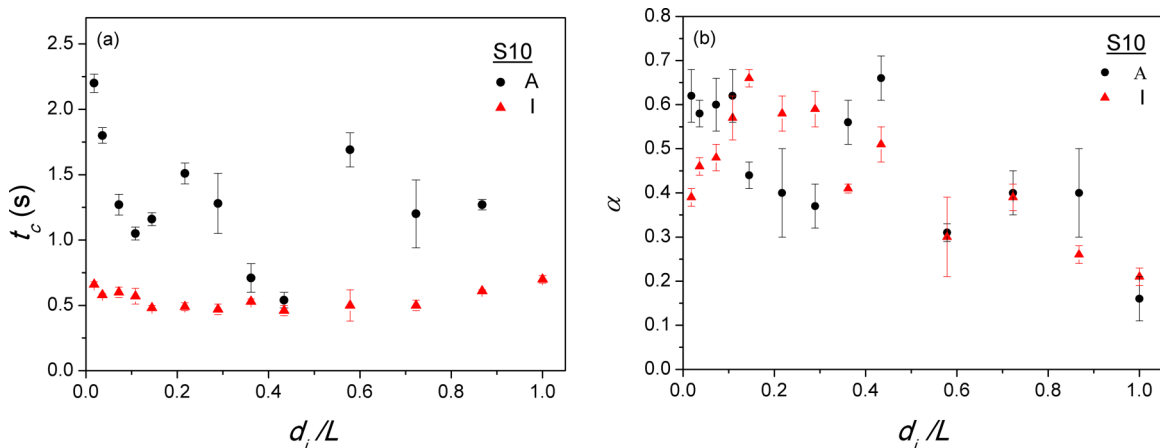


FIG. 20. (a) Characteristic transient time t_c and (b) the exponent α vs the ratio of the injection size d_i to the total length L for parameters sets A (black squares) and I (red triangles) with sample S10.

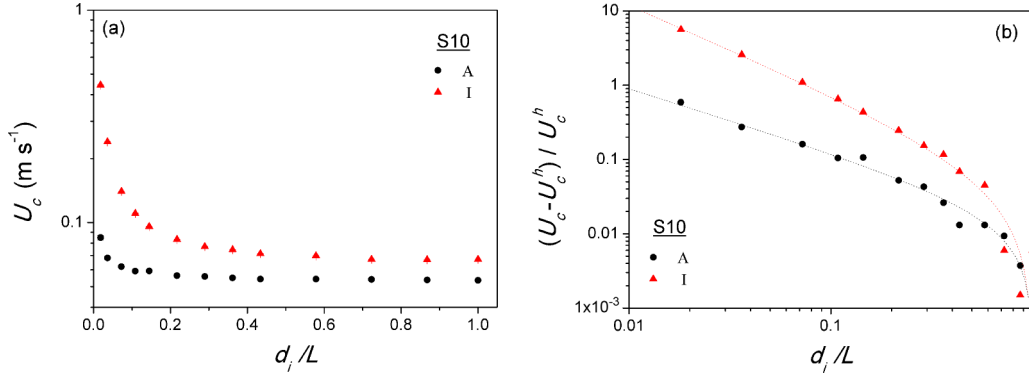


FIG. 21. (a) Critical velocity U_c vs the ratio of the injection size d_i to the total length L . (b) Plot of the relative gap $\frac{U_c - U_c^h}{U_c^h}$ vs d_i/L . The data presented are for parameters sets A (black squares) and I (red triangles) with sample S10. The dotted lines stand for Eq. (38) with exponents $\beta = 0.85$ (set A) and $\beta = 1.2$ (set I) and proportionality coefficients of 0.018 (set A) and 0.060 (set I).

mentioned before in Sec. IV A, another change in behavior was found regarding the existence of the *fluidized cavity* regime for the same parameters configurations that only differ by their viscosity.

This effect can also be highlighted here when the injection size d_i is varied. In that respect, phase diagrams were plotted in Fig. 22 reporting for five different sizes of injection d_i the domains of existence of the *static*, *fluidized cavity*, and *fluidized chimney* regimes.

The results shown in this figure, especially in Fig. 22(b), first confirm that the *fluidized cavity* state is significantly promoted at smaller injection sizes while it logically disappears as the lateral extent d_i of the upward fluid flow tends to the length of the sample (i.e., homogeneous and uniform fluidization). This finding is fairly consistent with the interpretation in terms of arching effect in the upper layer of the sample since this mechanism is obviously stronger for a smaller injection width. Moreover, it is also inferred from Fig. 22 that the *fluidized cavity* regime is hardly encountered in the higher viscosity configuration (parameter set A) and this new evidence of the influence of fluid viscosity will be discussed more in depth later, together with the previous reported signs of this viscosity effect.

V. DISCUSSION

A. Synthetic comparison to previous experiments

Generally speaking, the present numerical results are nicely consistent with the experimental phenomenology of localized fluidization previously mentioned in earlier papers

[22–24,34,37,38]. The three different stationary regimes were recovered, namely *static*, *fluidized cavity*, and *fluidized chimney* as final sample’s state after each simulation of 10 s. A difference shall be drawn about the *fluidized cavity* state that was systematically observed in the previous experiments whereas, in the present study, it was detected only for a very small fluid viscosity, here $\nu_f = 2 \times 10^{-6} \text{ m}^2 \text{ s}^{-1}$, but disappeared for a large viscosity, namely $\nu_f = 5 \times 10^{-5} \text{ m}^2 \text{ s}^{-1}$. Yet the previous experiments which have highlighted the existence of the *fluidized cavity* have used liquids with either intermediate and higher viscosity values, namely water ($\nu_f \sim 10^{-6} \text{ m}^2 \text{ s}^{-1}$) [22–24] and index-matched oil mixture ($\nu_f \sim 3 \times 10^{-5} \text{ m}^2 \text{ s}^{-1}$) [37,38].

Regarding more specifically the critical velocity for fluidized chimney, a simple proportionality relation with the initial bed’s height H_0 was found both qualitatively, by construction of phase diagrams where almost linear frontiers can be observed, and quantitatively, by a systematic analysis of the critical chimney velocity U_c deduced from divergence of the duration t_0 of the transient regime to fluidized chimney (see Sec. IV B). As already mentioned in Sec. IV A, this linear dependence is consistent with the first experiments of localized fluidization [22,23,34,38] whereas a more recent study has shown that this relation progressively saturates for larger bed heights, as the situation tends to the more usual case of homogeneous fluidization [37]. It is likely that this saturation should be recovered numerically for larger systems that have unfortunately not been simulated here for computational time limitations. Note also that He and coauthors [23]

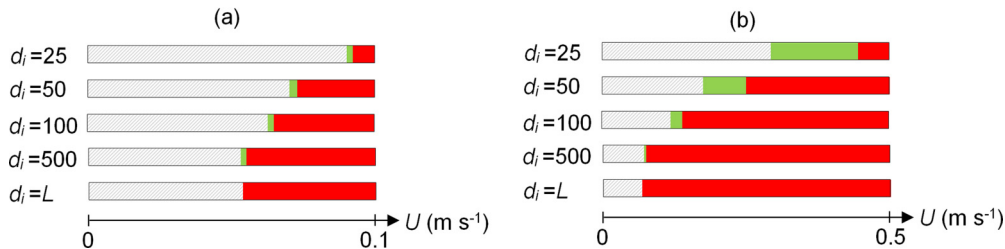


FIG. 22. Phase diagrams discriminating for five different injection sizes d_i , namely $d_i/L = 0.018, 0.036, 0.072, 0.36,$ and 1 (with L being the sample lateral length) and different steady states obtained with sample S10: (a) parameters set A ($\nu_f = 5 \times 10^{-5} \text{ m}^2 \text{ s}^{-1}$) and (b) parameters set I ($\nu_f = 2 \times 10^{-6} \text{ m}^2 \text{ s}^{-1}$). The *static*, *fluidized cavity*, and *fluidized chimney* regimes are in hatched gray, light green, and red, respectively.

adapted further the model initially proposed in Ref. [34] and found an analytical expression that appears to be consistently almost linear with the bed height. However, no saturation was observed in their experiments where a somewhat different geometry and hydrodynamic conditions were used. Note that the 3D numerical model by Tang and coauthors [43] correctly predicted these experimental data and the linear dependence on the bed height.

Previous experiments [37,38] are also in qualitative agreement with the observed hysteresis effect, when sequences during injection velocity increase and decrease back. This brings to the definition of a fourth memory-dependent steady-state regime, referred to as *potential fluidized cavity*. This regime is observed when a first chimney fluidization within the sample occurs and it allows for a fluidized area to be observed significantly below the critical velocity at which the first local fluidization would be detected during a simple velocity increase phase. As will be discussed hereafter in Sec. VB, it should be underlined that, quantitatively, the hysteresis effect simulated in the present study is noticeably less pronounced than highlighted by the experimental results.

Given the lack of experimental data, the present comprehensive analysis of the transient regime to fluidized chimney presented in Sec. IVB is essential for our current understanding of its scaling with various system parameters. In this comparison with previous experiments, it was found that the divergence of transient time t_0 with the injection velocity U is compatible with the empirical expression given by Eq. (28). This result is very similar to the scaling proposed by Philippe and Badiane [38] in the laminar flow regime, except that the exponent α was around 1.0 in the experiments and rather close to 0.6 in the present study. In addition, it has been shown from these experimental data that the critical chimney velocity U_c simply scales with the Stokes velocity [38], and in particular $U_c \propto d^2$. The empirical scaling supplied by our numerical simulations, namely $U_c \propto d^{5/4}$, was *a priori* different but can in fact be consistently rationalized with Stokes law from an Ergun-type relation (adapted to our two-dimensional system). Indeed, following this expression, the quadratic contribution of the Ergun law [see Eq. (35)], that remained almost negligible in the experiments where the Reynolds number Re did not exceed 10, seemed essential in the simulations having Re values up to 240. The proposed 2D version of the Ergun law was actually in reasonable agreement with our data as shown in Fig. 16(a). On the contrary, for high-Reynolds-number conditions, as in the experiments of Alsaydalani and coauthors [22] and related simulations by Tang and coauthors [43] where $Re > 1,000$, reanalyzing the data of fluidization onset suggests that the critical velocity at injection is approximately proportional to the grain diameter to a power around 0.8. This result consistently confirms a regular reduction of the d exponent with Re until a fully turbulent case where one can reasonably expect U_c to be proportional to $\sqrt{g^*d}$, or equivalently $Ar \propto Re_c^2$. This would also corresponds to a “constant” (i.e., apart from dependence on d_i and H) densimetric Froude number [43].

The last contribution of the present study to better insight of localized fluidization within a granular bed concerned the influence of d_i , the lateral extent at fluid flow injection. Previous experimental studies have tested the impact of the

injection width using different nozzle sizes: 3, 15, and 35 mm in the experiments of Zoueshtiagh and Merlen [34]; 6 and 14 mm in the experiments of Philippe and Badiane [38]; and 10, 20, 30, and 40 mm in the more recent work by Mena and coworkers [37]. Furthermore, one can cite the experiments of Alsaydalani and coauthors [22] using a rectangular source with a constant width and a small aperture $d_i = 0.33, 0.62,$ and 0.92 mm. A consensual outcome was that the influence of the nozzle diameter remained weak, if not negligible, on the critical flow rate at fluidized chimney onset. As shown in Sec. IV C, the same does not hold for our numerical results where clearly neither the critical velocity U_c nor a 2D-adapted flow rate $d_i \times U_c$ could be considered as constant.

This discrepancy should, however, be understood in terms of the system dimensions. Indeed, compared to the total lateral length of the granular sample, the ranges of injection widths explored in the experiments remained quite limited and did not exceed a ratio $d_i/L < 0.2$. Yet, if the injection flow inlet continuously tends to the dimensions of the sample ($d_i \rightarrow L$), the classical situation of homogeneous and uniform fluidization is recovered, imposing therefore a constant critical velocity condition U_c^h at onset (see Sec. IV C). Consequently, the apparent invariance of the critical flow rate inferred from the experimental results obviously fails to predict fluidization threshold when increasing further the injection size. This suggests that, in the experiments, the injection velocity shall first decrease almost as d_i^{-2} (i.e., almost constant critical flow rate) and then progressively saturates to the asymptotic value U_c^h . Converted to our two-dimensional system, the same projection remains valid for U_c but now with a starting decrease in d_i^{-1} . This kind of behavior is indeed consistent with our results as evidenced by the empirical law proposed in Eq. (38), where the exponent β was actually very close to 1. A dependance of U_c on d_i^{-1} is also rather consistent with the 2D numerical model by Tang and coauthors [43] and with the 3D experimental results of Alsaydalani and coworkers [22] based on a rectangular source of varying small aperture d_i .

B. Influence of the 2D geometry

The main drawback of the present DEM-LBM simulations most probably lies in the restriction of the model to a 2D geometry. Nevertheless, this simplification was strictly necessary in view of the goals of this study. Our key objective was indeed first directed toward an extensive comprehensive study and a systematic analysis of the influence of the various parameters of the system. At the same time, we had in mind the opportunity to study macroscopic samples, containing a rather large number of grains, up to 5000 individual particles. To fully achieve this task, more than 900 independent simulations were run for, in most cases, durations of 10 s in physical time. The present computations performed separately on one thread of a calculation server (2.4-GHz processors) have required typically from 96 to 120 h (4 to 5 days) for each of them and have generated a huge amount of data. It is therefore easier to realize that an extension to 3D was absolutely incompatible with the original goals and objectives that motivated this study.

That being said, we believe that some already mentioned limitations of the present modeling come from the two-dimensional nature of our simulated systems. In terms of the

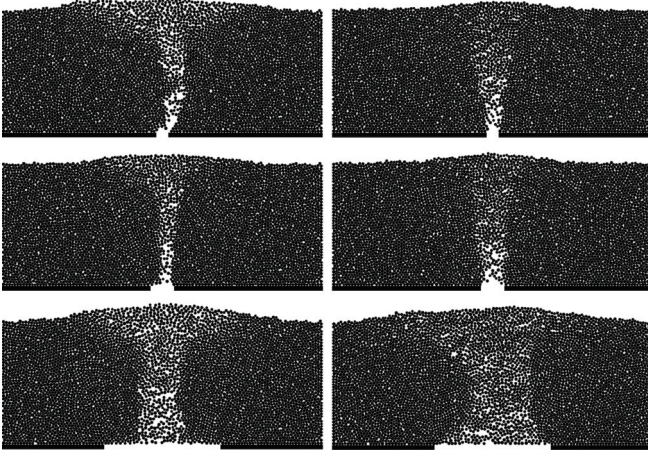


FIG. 23. Shape of the *fluidized chimney* steady-state, for $d_i/L = 0.036, 0.072$, and 0.36 (from top to bottom), obtained with sample S10: (left) parameter set A ($\nu_f = 5 \times 10^{-5} \text{ m}^2 \text{ s}^{-1}$) and (right) parameter set I ($\nu_f = 2 \times 10^{-6} \text{ m}^2 \text{ s}^{-1}$).

general mechanical behavior of the grains, the 2D geometry reduces the degrees of freedom accessible for the particles and should *a priori* contribute to enhanced hysteresis effects compared to the real 3D experimental observations. However, some hydrodynamic implications must also be taken into account, which could possibly minimize the hysteresis effects. First, resulting from the use of the hydraulic radius in the LBM calculation (see Sec. IIC), the 2D porous system has a rather large permeability value due to a substantially artificial pores network with no contact or even small constrictions between particles. Moreover, regarding the porous flow within the granular bed, the upward injection flow diffuses only laterally in the numerical two-dimensional system, and not radially in the whole 3D space. The velocity magnitude consequently decreases more slowly away from the source comparatively to the actual 3D case. Lastly, the periodic boundary conditions imposed on top and bottom of the integration domain (see Fig. 8) further mitigate the lateral expansion of the flow, especially when the injection width remains rather small, and tend to concentrate even more the flow, especially for small injection width conditions. To conclude, granular mechanical behavior and porous flow provide complementary and possibly opposite contributions to the existence of arching in 2D and there is consequently no clear explanation for the discrepancy reported in Sec. IVC between the present modeling and the previous experimental results from the literature, in this specific range $d_i/L < 0.2$.

C. Role of the hydrodynamic regime in the cavity

The previous assumption that the upward porous flow remains highly focused is further supported by a closer analysis of the evolution of the fluidized area versus injection width increase. For this, the final shape of the assumed stationary fluidized chimney is plotted in Fig. 23, for sample S10 and parameter sets A and I, and for three different values of the injection width d_i . We see that the lateral extent of the chimney is roughly constant with height, except close to the upper surface, and increases with the injection width d_i . However,

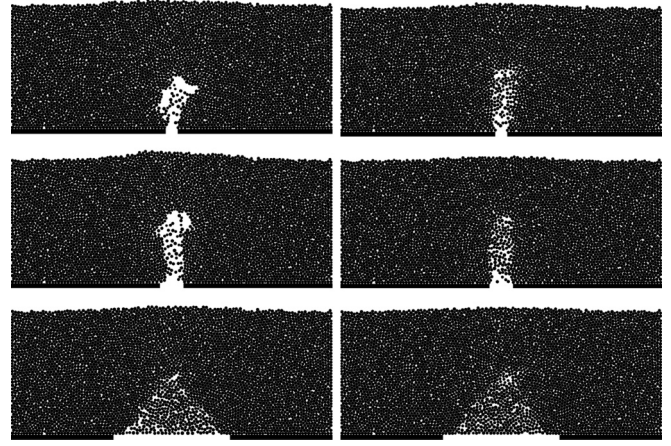


FIG. 24. Shapes of the fluidized zone during the transient regime, at the position where the fluidized height is almost half the initial bed height ($H_f/H_0 \sim 0.5$), for $d_i/L = 0.036, 0.072$, and 0.36 (from top to bottom), obtained with sample S10: (left) parameter set A ($\nu_f = 5 \times 10^{-5} \text{ m}^2 \text{ s}^{-1}$) and (right) parameter set I ($\nu_f = 2 \times 10^{-6} \text{ m}^2 \text{ s}^{-1}$).

the chimney diameter D_{ch} widens quite slowly and much less rapidly than d_i , especially in the small injection widths region. In particular, that means D_{ch} clearly does not scale with d_i . Moreover, regarding the influence of the fluid viscosity, it fairly appears in Fig. 23 that, for a given injection width d_i , the fluidized chimney is narrower for $\nu_f = 5 \times 10^{-5} \text{ m}^2 \text{ s}^{-1}$ than for $\nu_f = 2 \times 10^{-6} \text{ m}^2 \text{ s}^{-1}$. By now, we do not have any physical explanation for this result but, obviously, it directly explains why the critical velocity U_c departs more sharply from U_c^h when the fluid has a smaller viscosity as highlighted in Sec. IVC. Indeed, considering that the critical velocity U_c^h is almost reached in the chimney and assuming roughly a flow rate balance at injection source and inside the fluidized chimney, fluidization of a narrow zone (here for $\nu_f = 5 \times 10^{-5} \text{ m}^2 \text{ s}^{-1}$) requires a smaller injection velocity U_c compared to the situation of a significantly larger fluidized width (here for $\nu_f = 2 \times 10^{-6} \text{ m}^2 \text{ s}^{-1}$). It should, however, be noted that this explanation is unfortunately insufficient since it does not predict a difference between the two cases as large as that reported in Fig. 21.

Of great and probably even further interest is also the shape of the expanding fluidized cavity during the transient regime, as reported in Fig. 24, here again for sample S10 and parameters sets A and I as well as for the same three injection sizes d_i as reported in Fig. 23.

Interestingly, the difference observed in the final steady state with regard to the size of the fluidized chimney proves to be not yet notable during the transient regime, and there does not even appear to have any strong influence of the injection width d_i in this regime, at least for what concerns the size of the top of the fluidized zone. The only difference lies in the shape of this zone which evolves from almost rectangular for small injection size to triangular at larger d_i values. But the typical size at the roof of the fluidized expanding area appears to be almost the same in all cases, namely $L_{\text{cav}} \sim 10d$.

On the contrary, what seems to differ here is the interior of the fluidized area, most specifically in the range of small injection size since both triangular fluidized cavity are very similar

for $d_i/L = 0.36$ whatever the fluid viscosity. In the other cases, there are few fluidized particles inside the expanding cavity at high fluid viscosity whereas a substantially denser cloud of moving grains is observed at smaller viscosity. This must be directly related to the hydrodynamic conditions inside the fluidized cavity. Considering here again that the fluid velocity inside the fluidized area is close U_c^h , one can then define a typical Reynolds number of the cavity as follows:

$$\text{Re}_{\text{cav}} = \frac{U_c^h L_{\text{cav}}}{\nu_f}. \quad (39)$$

Then, an actually small Reynolds number is obtained for $\nu_f = 5 \times 10^{-5} \text{ m}^2 \text{ s}^{-1}$, $\text{Re}_{\text{cav}} \sim 20$, while a significantly higher value is found for $\nu_f = 2 \times 10^{-6} \text{ m}^2 \text{ s}^{-1}$, $\text{Re}_{\text{cav}} \sim 600$.

This variation in hydrodynamic regimes supports the idea that two distinct scenarios of localized fluidization could be proposed. When examining closely our simulations during the transient regime leading either to a *fluidized cavity* or, in most cases, to a *fluidized chimney*, the upward expansion of the fluidized zone seems to be created by an overall uplift of the upper layer of the sample, induced by fluid overpressure. It might then be thought that the group of grains above the top of the fluidized cavity quickly gets locally unstable, but in way that depends on the hydrodynamic regime in the cavity.

At small Reynolds numbers, the fluid flow through the cavity that remains laminar enables the existence of well-defined frontiers between the particle-poor cavity and the surrounding dense and almost static grain packing. It is likely that the roof of the expanding cavity behaves more or less as a rigid body and destabilizes by tilting to one side, generating at the other side an inclined fracture of limited extent. The fluidized zone would thus successively move forward, broadly in the vertical direction and more or less rapidly according to the magnitude of the injection velocity. Moreover, once the fluid overpressure is high enough to generate the first fracture, the cavity expansion process is engaged and one can assume that this process will progress regularly until reaching the top of the sample. In some cases, a lateral side closure of the fluidized conduit could be observed in its upper part, but only for a short period. Besides, the same side closure process can also be noticed during the decreasing sequence in the hysteresis simulations at the time of the transition from chimney to cavity.

On the contrary, at higher Reynolds numbers, the fluid flow within the cavity is more turbulent and consequently removes many grains from the lateral dense area that remain later suspended in the fluidized zone. This induces more flow dissipation and much particle agitation, in the conduit but also nearby, with the frontiers between dense and dilute zones getting blurred. So the grains constituting the cavity roof are prone to collapse downward under the combined action of the fluid flow and collisions with particles in suspension. Then the fluidized zone progressively expands almost vertically. But, in these conditions, it is also likely that several previously eroded grains can get blocked against particles already at rest, preferentially at the top front of the fluidized cavity, creating a new cavity roof. This purely hydrodynamic mechanism seems capable of moderating the fluidization expansion or even stopping it. The latter case gives rise therefore to the *fluidized cavity* state where grains are regularly and almost

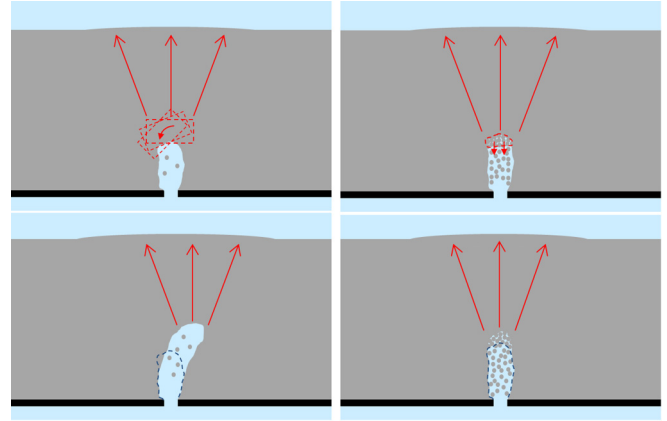


FIG. 25. Sketches illustrating the two scenarios of fluidized cavity upward expansion proposed for both (left) laminar regime ($\text{Re}_{\text{cav}} \sim 20$) and (right) turbulent regime ($\text{Re}_{\text{cav}} \sim 600$) of the fluid flow within the cavity.

steadily removed and blocked again at the cavity roof. This also explains why fluctuations of the fluidized zone have been reported (see Sec. IV A).

These physically plausible interpretations are illustrated in Fig. 25. They could explain the influence of the fluid viscosity reported several times in this numerical study. More than the fluid viscosity, the key parameter is actually the hydrodynamic regime within the fluidized cavity in upward expansion, characterized as we have seen by a typical Reynolds number Re_{cav} that switches between 20 to 600 with the parameters used in the related simulations. A last remaining question concerns the comparison of our simulations to previous experiments and, for that, the corresponding values of Re_{cav} are needed. Referring to Ref. [37], the diameter of the steady fluidized chimney seems to scale with the grain diameter d , namely $D_{\text{ch}} \sim 6d$, and can be used as the typical size of the localized fluidization. Additionally, from the critical flow rate Q_{ch} at chimney onset, a characteristic velocity is obtained: $U_{\text{ch}} = 4Q_{\text{ch}}/(\pi D_{\text{ch}}^2)$. Then the typical Reynolds number in the fluidized cavity is

$$\text{Re}_{\text{cav}} = \frac{U_{\text{ch}} D_{\text{ch}}}{\nu_f} \sim \frac{2Q_{\text{ch}}}{3\pi d\nu_f}. \quad (40)$$

Based on the experimental data in Ref. [37] with a rather viscous liquid, it can be stated that Re_{cav} ranges typically between 100 and 300, and substantially higher values of Re_{cav} will be found for other experiments using water as liquid [23]. The corresponding cavity hydrodynamic regimes are consequently somewhat closer to the numerical configuration with a viscosity equal to $\nu_f = 2 \times 10^{-6} \text{ m}^2 \text{ s}^{-1}$ (parameter set D) and indeed, in this case, the *fluidized cavity* regime is actually observed and the hysteresis appears stronger, in agreement with the previous experimental findings. This last point supports and strengthens our interpretation that remains nonetheless conditional and needs to be further confirmed later on.

VI. CONCLUSION

To briefly conclude, our numerical model allows for an efficient computation of particle-laden fluids. It combines discrete element and lattice Boltzmann methods, coupled

together in a two-dimensional geometry. After a successful validation by comparison to different benchmarks, namely lid-driven cavity flow and sedimentation flow of a circular cylinder, the numerical model was used to perform an extensive investigation of localized fluidization induced by an upward fluid flow injection underneath a granular bed. It clearly demonstrated its ability to satisfactorily simulate the main physical phenomena involved in this specific situation. By analyzing a large number of extensive simulations (more than 900) with various sets of bed heights, injection sizes, and physical parameters, many results were obtained, including consistent comparisons with previous experiments as well as insights on some specific points. The major outcomes of this study are summarized hereafter:

(1) The model is able to reproduce the general phenomenology reported in several previous experiments, especially in terms of the three final stationary states of localized fluidization: *static*, *fluidized cavity*, and *fluidized chimney* regimes, that have all been recovered.

(2) New specific features of the *fluidized cavity* regime were highlighted, regarding its range of existence versus injection velocity. It was observed indeed that this range increases with bed's height while it decreases both with injection size and even more with fluid viscosity. The *fluidized cavity* state was, for instance, hardly if ever obtained in computations where the fluid viscosity was 50 times higher than that of water.

(3) Although less pronounced than in real 3D experiments, a notable hysteresis effect was observed in the simulations and a typical picture of the normal force network within the sample supported the previously proposed explanation based on arching mechanism. Limitations arising from the 2D geometry of the model are believed to be responsible for the reduced strength observed here.

(4) The transient regime toward *fluidized chimney* was quantitatively and systematically analyzed. Compared to previous experimental works, the same qualitative power-law divergence of the duration time t_0 with injection velocity U was obtained but with an exponent closer to 0.6 than 1, as reported in the experiments. This divergence law has helped to provide characteristic injection velocity U_c and expansion time t_c for eleven different sets of physical parameters. Once converted into dimensionless groups, namely $Re_c = U_c d / \nu_f$ and $\tau_c = t_c \nu_f / d^2$, a general collapse was obtained for Re_c and τ_c against Archimedes number Ar ($Ar = g^* d^3 / \nu_f$ with g^* being the reduced gravity). An empirical power law seemed to satisfactorily describe the data while a more physically sound relation was also proposed, based on an Ergun-like expression, and showed reasonable agreement.

(5) The mean expansion rate before the system reaches a steady fluidized chimney, defined as $V_0 = H_0 / t_0$, was shown to follow a dimensionless power law relation, namely

$V_0 / U_c \propto (U / U_c - 1)^{3/5}$, where a remaining dependency to the initial bed's height was only found in value of the proportionality coefficient.

(6) An original and rather comprehensive study focused on the influence of the injection size on the transient regime. The characteristic transient time t_c and the exponent α showed large fluctuations but seemed, however, to remain more or less constant, except for α that ultimately decreased, typically from 0.6 to 0.2, when the injection width approached the total sample's length L . As described by an empirical dimensionless scaling, the critical velocity U_c first decreased with the injection size roughly as the power of -1 before it progressively saturated to the final homogeneous fluidization value U_c^h . As discussed here, this behavior appeared consistent with previous experimental results given the two dimensionality of the present model. The observed gap between U_c and U_c^h was substantially higher when the fluid viscosity used was decreased.

(6) Finally, from a careful and detailed analysis of all the simulations carried out in the present study, a tentative explanation was proposed for most of the differences observed between experimental and numerical findings, especially with respect to the dependence on fluid viscosity and existence of the *fluidized cavity* state. The upward expansion process of the fluidized zone was consistently assumed to be directly related to the prevailing hydrodynamic regime within the expanding cavity. In laminar conditions, obtained here for a high-viscosity fluid and typical Reynolds numbers of 20 inside the expanding cavity, an almost void conduit was observed that seems to progress by successive steps, due to local destabilization of the cavity roof that, under the uplift action of the fluid overpressure, tilts on one side as a rigid body and consequently generates an opening in the granular structure at the other side. In more turbulent conditions, here at smaller viscosity and typical Reynolds numbers around 600, the grains at the cavity roof easily collapse downward by both the action of the agitated fluid flow and the collisions of grains in suspension within the fluidized zone. The fluidized area expands upward more straightly but can be slowed down, or even stopped, by the reverse blockage of eroded grains at the cavity roof. This thus explains a greater propensity to *fluidized cavity* regime in the turbulent flow scenario contrary to the laminar one. Typical cavity Reynolds numbers from 100 to 300, and even more, in the previous experiments have consistently suggested that the turbulent flow scenario was indeed the most relevant one in the experimental conditions.

ACKNOWLEDGMENTS

This work benefits from fruitful discussions with Z. Benseghier, P. Cuéllar, M. Nicolas, V. Richefeu, and L. Sibille.

- [1] M. L. Passos, G. Masarani, J. T. Freire, and A. S. Mujumdar, Drying of pastes in spouted beds of inert particles: Design criteria and modeling, *Drying Technol.* **15**, 605 (1997).
 [2] E. G. Pereira, J. N. da Silva, J. L. de Oliveira, and C. S. Machado, Sustainable energy: A review of gasification technologies, *Renew. Sustain. Energy Rev.* **16**, 4753 (2012).

- [3] R. Warnecke, Gasification of biomass: Comparison of fixed bed and fluidized bed gasifier, *Biomass Bioenergy* **18**, 489 (2000).
 [4] K. Smolders and J. Baeyens, Elutriation of fines from gas fluidized beds: Mechanisms of elutriation and effect of freeboard geometry, *Powder Technol.* **92**, 35 (1997).

- [5] C. Y. Wen and L. H. Chen, Fluidized-bed freeboard phenomena—Entrainment and elutriation, *AIChE J.* **28**, 117 (1982).
- [6] J. M. Link, L. A. Cuypers, N. G. Deen, and J. A. M. Kuipers, Flow regimes in a spout-fluid bed: A combined experimental and simulation study, *Chem. Eng. Sci.* **60**, 3425 (2005).
- [7] V. S. Sutkar, N. G. Deen, and J. A. M. Kuipers, Spout fluidized beds: Recent advances in experimental and numerical studies, *Chem. Eng. Sci.* **86**, 124 (2013).
- [8] Y. Peng and L. T. Fan, Hydrodynamic characteristics of fluidization in liquid-solid tapered beds, *Chem. Eng. Sci.* **54**, 2277 (1997).
- [9] R. N. Weismann and G. P. Lennon, Design of fluidizer systems for coastal environment, *J. Waterway, Port, Coastal, Ocean Eng.* **120**, 468 (1994).
- [10] F. Gallo and A. Woods, On steady homogeneous sand-water flows in vertical conduit, *Sedimentology* **51**, 195 (2004).
- [11] D. R. Lowe, Water escape structures in coarse-grained sediments, *Sedimentology* **22**, 157 (1975).
- [12] T. Mörz, E. A. Karlik, S. Kreiter, and A. Kopf, An experimental setup for fluid venting in unconsolidated sediments: New insights to fluid mechanics and structures, *Sediment. Geol.* **196**, 251 (2007).
- [13] R. J. Nichols, R. S. J. Sparks, and C. J. N. Wilson, Experimental studies of the fluidization of layered sediments and the formation of fluid escape structures, *Sedimentology* **41**, 233 (1994).
- [14] A. L. Walters, J. C. Phillips, R. J. Brown, M. Field, and T. M. Gernon, The role of fluidisation in the formation of volcaniclastic kimberlite: Grain size observations and experimental investigation, *J. Volcanol. Geotherm. Res.* **155**, 119 (2006).
- [15] L. A. Briens, C. L. Briens, A. Margaritis, S. L. Cooke, and M. A. Bergougnou, Characterization of channelling in multiphase systems: Application to a liquid fluidized bed of angular Biobone particles, *Powder Technol.* **91**, 1 (1997).
- [16] M. Söderlund, P. Bots, P. Eriksson, P. Nilsson, and J. Hartlen, Evaluating the domino effect of critical constructions due to damage of underground water pipelines, *Loss Prevention Bull.-Inst. Chem. Eng.* **195**, 22 (2007).
- [17] S. Bonelli, editor, *Erosion of Geomaterials* (Wiley-ISTE, New York, 2012).
- [18] S. Bonelli, editor, *Erosion in Geomechanics Applied to Dams and Levees* (John Wiley & Sons, New York, 2013).
- [19] C. S. P. Ohja, V. P. Singh, and D. D. Adrian, Determination of critical head in soil piping, *J. Hydraul. Eng.* **129**, 511 (2003).
- [20] J. B. Sellmeijer and M. A. Koenders, A mathematical model for piping, *Appl. Math. Model.* **15**, 646 (1991).
- [21] V. M. van Beek, H. Knoeff, and J. B. Sellmeijer, Observations on the process of backward erosion piping in small-, medium- and full-scale experiments, *Eur. J. Environ. Civ. En.* **15**, 1115 (2011).
- [22] M. O. A. Alsaydalani and C. R. I. Clayton, Internal fluidization in granular soils, *J. Hydraul. Eng.* **140**, 04013024 (2014).
- [23] Y. He, D. Z. Zhu, T. Zhang, Y. Shao, and T. Yu, Experimental observations on the initiation of sand-bed erosion by an upward water jet, *J. Hydraul. Eng.* **143**, 06017007 (2017).
- [24] Y. Tang, D. Z. Zhu, and D. H. Chan, Experimental study on submerged sand erosion through a slot on a defective pipe, *J. Hydraul. Eng.* **143**, 04017026 (2017).
- [25] J. E. van Zyl, M. O. A. Alsaydalani, C. R. I. Clayton, T. Bird, and A. Dennis, Soil fluidisation outside leaks in water distribution pipes: Preliminary observations, *Water Manag.-Proc. Inst. Civil Eng.* **166**, 546 (2013).
- [26] N. Almohammed, F. Alobaid, M. Breuer, and B. Epple, A comparative study on the influence of the gas flow rate on the hydrodynamics of a gas-solid spouted fluidized bed using Euler-Euler and Euler-Lagrange/DEM models, *Powder Technol.* **264**, 343 (2014).
- [27] T. M. Gernon, M. A. Gilbertson, R. S. J. Sparks, and M. Field, Gas-fluidisation in an experimental tapered bed: Insights into processes in diverging volcanic conduits, *J. Volcanol. Geotherm. Res.* **174**, 49 (2008).
- [28] T. M. Gernon and M. A. Gilbertson, Segregation of particles in a tapered fluidized bed, *Powder Technol.* **231**, 88 (2012).
- [29] M. S. van Buijtenen, W.-J. Dijk, N. G. Deen, J. A. M. Kuipers, T. Leadbeater, and D. J. Parker, Numerical and experimental study on multiple spout fluidized beds, *Chem. Eng. Sci.* **66**, 2368 (2011).
- [30] M. S. van Buijtenen, K. Buist, N. G. Deen, J. A. M. Kuipers, T. Leadbeater, and D. J. Parker, Numerical and experimental study on spout elevation in spout-fluidized beds, *AIChE J.* **58**, 2524 (2012).
- [31] O. Galland, G. R. Gisler, Ø. T. Haug, Morphology and dynamics of explosive vents through cohesive rock formations, *J. Geophys. Res.: Solid Earth* **119**, 4708 (2014).
- [32] P. Rigord, A. Guarino, V. Vidal, and J.-C. Géminard, Localized instability of a granular layer submitted to an ascending liquid flow, *Granular Matter* **7**, 191 (2005).
- [33] T. Wilhelm and K. Wilmański, On the onset of flow instabilities in granular media due to porosity inhomogeneities, *Int. J. Multiphase Flow* **28**, 1929 (2002).
- [34] F. Zoueshtigh and A. Merlen, Effect of a vertically flowing water jet underneath a granular bed, *Phys. Rev. E* **75**, 056313 (2007).
- [35] M. H. Köhl, G. Lu, J. R. Third, M. Häberlin, L. Kasper, K. P. Prüssmann, and C. R. Müller, Magnetic resonance imaging (MRI) study of jet formation in packed beds, *Chem. Eng. Sci.* **97**, 406 (2013).
- [36] M. H. Köhl, G. Lu, J. R. Third, K. P. Prüssmann, and C. R. Müller, Magnetic resonance imaging (MRI) of jet height hysteresis in packed beds, *Chem. Eng. Sci.* **109**, 276 (2014).
- [37] S. E. Mena, L.-H. Luu, P. Cuéllar, P. Philippe, and J. S. Curtis, Parameters affecting the localized fluidization in a particle medium, *AIChE J.* **63**, 1529 (2017).
- [38] P. Philippe and M. Badiane, Localized fluidization in a granular medium, *Phys. Rev. E* **87**, 042206 (2013).
- [39] R. Béguin, P. Philippe, and Y.-H. Faure, Pore-scale flow measurements at the interface between a sandy layer and a model porous medium: Application to statistical modeling of contact erosion, *J. Hydraul. Eng.* **139**, 1 (2013).
- [40] J. A. Dijkman, F. Rietz, K. A. Lorincz, M. van Hecke, and W. Losert, Refractive index matched scanning of dense granular materials, *Rev. Sci. Instrum.* **83**, 011301 (2012).
- [41] M. A. van der Hoef, M. van Sint Annaland, N. G. Deen, and J. A. M. Kuipers, Numerical simulation of dense gas-solid fluidized beds: A multiscale modeling strategy, *Annu. Rev. Fluid Mech.* **40**, 47 (2008).
- [42] N. G. Deen, M. Van Sint Annaland, M. A. Van der Hoef, and J. A. M. Kuipers, Review of discrete particle modeling of fluidized beds, *Chem. Eng. Sci.* **62**, 28 (2007).

- [43] Y. Tang, D. H. Chan, and D. Z. Zhu, Numerical investigation of sand-bed erosion by an upward water jet, *J. Eng. Mech.* **143**, 04017104 (2017).
- [44] F. Alobaid and B. Epple, Improvement, validation and application of CFD/DEM model to dense gas-solid flow in a fluidized bed, *Particuology* **11**, 514 (2013).
- [45] E. P. Montellà, M. Toraldo, B. Chareyre, and L. Sibille, Localized fluidization in granular materials: Theoretical and numerical study, *Phys. Rev. E* **94**, 052905 (2016).
- [46] H. Sari, B. Chareyre, E. Catalano, P. Philippe, and E. Vincens, Investigation of internal erosion processes using a coupled DEM-fluid method, in *Particle-Based Methods II: Fundamentals and Applications: Second International Conference on Particle-Based Methods, Fundamentals and Applications (Particles), Barcelona, Spain, October 26–28, 2011*, edited by E. Oñate and D. R. J. Owen (International Center for Numerical Methods in Engineering (CIMNE), Barcelona, Spain, 2011), pp. 820–830.
- [47] X. Cui, J. Li, A. Chan, and D. Chapman, A 2D DEM-LBM study on soil behaviour due to locally injected fluid, *Particuology* **10**, 242 (2012).
- [48] X. Cui, J. Li, A. Chan, and D. Chapman, Coupled DEM-LBM simulation of internal fluidisation induced by a leaking pipe, *Powder Technol.* **254**, 299 (2014).
- [49] D. F. Boutt, B. K. Cook, B. J. O. McPherson, and J. R. Williams, Direct simulation of fluid-solid mechanics in porous media using the discrete element and lattice Boltzmann methods, *J. Geophys. Res.: Solid Earth* **112**, B10209 (2007).
- [50] D. F. Boutt, B. K. Cook, and J. R. Williams, A coupled fluid-solid model for problems in geomechanics: Application to sand production, *Int. J. Numer. Anal. Methods Geomech.* **35**, 997 (2011).
- [51] D. R. J. Owen, C. R. Leonardi, and Y. T. Feng, An efficient framework for fluid-structure interaction using the lattice Boltzmann method and immersed moving boundaries, *Int. J. Numer. Methods Eng.* **87**, 66 (2011).
- [52] Y. Han and P. A. Cundall, LBM-DEM modeling of fluid-solid interaction in porous media, *Int. J. Numer. Anal. Methods Geomech.* **37**, 1391 (2013).
- [53] B. Bigot, T. Bonometti, L. Lacaze, and O. Thual, A simple immersed-boundary method for solid-fluid interaction in constant- and stratified-density flows, *Comput. Fluids* **97**, 126 (2014).
- [54] P. Mutabaruka, J.-Y. Delenne, K. Soga, and F. Radjaï, Initiation of immersed granular avalanches, *Phys. Rev. E* **89**, 052203 (2014).
- [55] J. J. Derksen, Simulations of granular bed erosion due to laminar shear flow near the critical Shields number, *Phys. Fluids* **23**, 113303 (2011).
- [56] H. M. D. Harshani, S. A. Galindo-Torres, A. Scheuermann, and H. B. Muhlhaus, Micro-mechanical analysis on the onset of erosion in granular materials, *Philos. Mag.* **95**, 3146 (2015).
- [57] F. Lominé, L. Scholtès, L. Sibille, and P. Poullain, Modeling of fluid-solid interaction in granular media with coupled lattice Boltzmann/discrete element methods: Application to piping erosion, *Int. J. Num. Anal. Methods Geomech.* **37**, 577 (2013).
- [58] M. Mansouri, J.-Y. Delenne, M. S. El Youssoufi, and A. Séridi, A 3D DEM-LBM approach for the assessment of the quick condition for sands, *C. R. Mécanique* **337**, 675 (2009).
- [59] S. Succi, *The Lattice Boltzmann Equation for Fluid Dynamics and Beyond* (Oxford University Press, New York, 2001).
- [60] M. C. Sukop and D. T. Thorne, *Lattice Boltzmann Modeling: An Introduction for Geoscientists and Engineers* (Springer, Berlin, 2007).
- [61] X. He and L.-S. Luo, Theory of the lattice Boltzmann equation: From Boltzmann equation to lattice Boltzmann equation, *Phys. Rev. E* **56**, 6811 (1997).
- [62] X. He and L.-S. Luo, *A priori* derivation of the lattice Boltzmann equation, *Phys. Rev. E* **55**, R6333(R) (1997).
- [63] P. L. Bhatnagar, E. P. Gross, and M. Krook, A model for collision processes in gases, I: Small amplitude processes in charged and neutral one-component systems, *Phys. Rev.* **94**, 511 (1954).
- [64] Y. H. Qian, D. d’Humières, and P. Lallemand, Lattice BGK models for Navier-Stokes equation, *Europhys. Lett.* **17**, 479 (1992).
- [65] S. Chapman and T. G. Cowling, *The Mathematical Theory of Nonuniform Gases* (Cambridge University Press, Cambridge, UK, 1970).
- [66] H. Chen, S. Chen, and W. H. Matthaeus, Recovery of Navier-Stokes equations using a lattice-gas Boltzmann method, *Phys. Rev. A* **45**, R5339(R) (1992).
- [67] D. d’Humières, I. Ginzburg, M. Krafczyk, P. Lallemand, and L.-S. Luo, Multiple-relaxation-time lattice Boltzmann models in three dimensions, *Philos. Trans. R. Soc. London, Ser. A* **360**, 437 (2002).
- [68] P. Lallemand and L.-S. Luo, Theory of the lattice Boltzmann method: Dispersion, dissipation, isotropy, Galilean invariance and stability, *Phys. Rev. E* **61**, 6546 (2000).
- [69] L.-S. Luo, W. Liao, X. Chen, Y. Peng, and W. Zhang, Numerics of the lattice Boltzmann method: Effects of collision models on the lattice Boltzmann simulations, *Phys. Rev. E* **83**, 056710 (2011).
- [70] Q. Zou and X. He, On pressure and velocity boundary conditions for the lattice Boltzmann BGK model, *Phys. Fluids* **9**, 1591 (1997).
- [71] C. K. Aidun, Y. Lu, and E. G. Ding, Direct analysis of particulate suspensions with inertia using the discrete lattice Boltzmann equation, *J. Fluid Mech.* **373**, 287 (1998).
- [72] S. Chen and G. D. Doolen, Lattice Boltzmann method for fluid flows, *Annu. Rev. Fluid Mech.* **30**, 329 (1998).
- [73] I. Ginzburg and D. d’Humières, Morphology and dynamics of explosive vents through cohesive rock formations, *Phys. Rev. E* **68**, 066614 (2003).
- [74] A. Ladd, Numerical simulations of fluid-particulate suspensions via a discretized Boltzmann equation (part I and II), *J. Fluid Mech.* **271**, 285 (2001).
- [75] A. Ladd and R. Verberg, Lattice Boltzmann simulations of particle-fluid suspensions, *J. Stat. Phys.* **104**, 1191 (2001).
- [76] P. A. Cundall and O. D. Strack, A discrete numerical model for granular assemblies, *Geotechnique* **29**, 47 (1979).
- [77] K. L. Johnson, *Contact Mechanics* (Cambridge University Press, London, 1985).
- [78] A. Di Renzo and F. P. Di Maio, Comparison of contact-force models for the simulation of collision in DEM-based granular flow codes, *Chem. Eng. Sci.* **59**, 525 (2004).
- [79] M. H. Sadd, Q. M. Tai, and A. Shukla, Contact law effects on wave propagation in particulate materials using distinct element modeling, *Int. J. Non-Linear Mech.* **28**, 241 (1993).

- [80] J. Schafer, S. Dippel, and D. Wolf, Force schemes in simulation of granular materials, *J. Phys. I (France)* **6**, 5 (1996).
- [81] J. M. Ting, M. Khwaja, L. R. Meachum, and J. D. Rowell, An ellipse-based discrete element model for granular materials, *Int. J. Num. Anal. Methods Geomech.* **7**, 603 (1993).
- [82] O. R. Walton, Numerical simulations of inelastic frictional particle-particle interactions, in *Particulate Two Phase Flow* (Butterworth-Heinemann, Boston, 1992).
- [83] Y. Tsuji, T. Kawaguchi, and T. Tanaka, Discrete particle simulation of two-dimensional fluidized bed, *Powder Technol.* **77**, 79 (1993).
- [84] C. O'Sullivan and J. D. Bray, Selecting a suitable time step for discrete simulations that use the central difference time integration scheme, *Eng. Comput.* **21**, 278 (2004).
- [85] Y. T. Feng, K. Han, and D. R. J. Owen, Coupled lattice Boltzmann method and discrete element modeling of particle transport in turbulent fluid flows: Computational issues, *Int. J. Num. Meth. Eng.* **72**, 1111 (2007).
- [86] K. Han, Y. T. Feng, and D. R. J. Owen, Coupled lattice Boltzmann and discrete element modeling of fluid-particle interaction problems, *Comput. Struct.* **85**, 1080 (2007).
- [87] M. Bouzidi, M. Firdaouss, and P. Lallemand, Momentum transfer on a Boltzmann lattice fluid with boundaries, *Phys. Fluids* **13**, 3452 (2002).
- [88] B. K. Cook, D. R. Noble, and J. R. Williams, A direct simulation method for particle-fluid systems, *Eng. Comput.* **21**, 151 (2004).
- [89] D. Z. Yu, R. W. Mei, L.-S. Luo, and W. Shyy, Viscous flow computations with the method of lattice Boltzmann equation, *Prog. Aero. Sci.* **39**, 329 (2003).
- [90] Z. G. Feng and E. E. Michaelides, The immersed boundary lattice Boltzmann methods for solving fluid particles interaction problems, *J. Comput. Phys.* **195**, 602 (2004).
- [91] D. R. Noble and R. Torczynski, A lattice Boltzmann method for partially saturated cells, *Int. J. Mod. Phys. C* **9**, 1189 (1998).
- [92] S. A. Galindo-Torres, A coupled discrete element lattice Boltzmann method for the simulation of fluid-solid interaction with particles of general shapes, *Comput. Methods Appl. Mech. Eng.* **265**, 107 (2014).
- [93] P. Lallemand and L.-S. Luo, Lattice Boltzmann method for moving boundaries, *J. Comput. Phys.* **184**, 406 (2003).
- [94] M. Mansouri, J.-Y. Delenne, and M. S. El Youssefi, A numerical model for the computation of permeability of cemented granular material, *Powder Technol.* **208**, 532 (2011).
- [95] D. K. Tran, N. Prime, F. Froiio, C. Callari, and E. Vincens, Numerical modelling of backward front propagation in piping erosion by DEM-LBM coupling, *Eur. J. Env. Civ. Eng.* **21**, 960 (2017).
- [96] U. Ghia, K. N. Ghia, and C. T. Shin, High-Re solutions for incompressible flow using the Navier-Stokes equations and a multigrid method, *J. Comput. Phys.* **48**, 387 (1982).
- [97] D. A. Perumal and A. K. Dass, Application of lattice Boltzmann method for incompressible viscous flows, *Appl. Math. Model.* **37**, 4075 (2012).
- [98] A. E. Hamielec and J. D. Raal, Numerical studies of viscous flow around circular cylinders, *Phys. Fluids* **12**, 11 (1969).
- [99] H. Takami and H. B. Keller, Steady two-dimensional viscous flow of an incompressible fluid past a circular cylinder, *Phys. Fluids* **12**, II51 (1969).
- [100] S. C. Dennis and G.-Z. Chang, Numerical solutions for steady flow past a circular cylinder at Reynolds numbers up to 100, *J. Fluid Mech.* **42**, 471 (1970).
- [101] B. Fornberg, A numerical study of steady viscous flow past a circular cylinder, *J. Fluid Mech.* **98**, 819 (1980).
- [102] D. J. Tritton, Experiments on the flow past a circular cylinder at low Reynolds numbers, *J. Fluid Mech.* **6**, 547 (1959).
- [103] S. Sen, S. Mittal, and G. Biswas, Steady separated flow past a circular cylinder at low Reynolds numbers, *J. Fluid Mech.* **620**, 89 (2009).
- [104] A. Ben Richou, A. Ambari, and J. K. Naciri, Drag force on a circular cylinder midway between two parallel plates at very low Reynolds numbers, part 1: Poiseuille flow (numerical), *Chem. Eng. Sci.* **59**, 3215 (2004).
- [105] J. Ngoma, P. Philippe, S. Bonelli, P. Cuéllar, J.-Y. Delenne, and F. Radjaï, Transient regime to fluidized chimney within a granular bed by means of 2D DEM/LBM modeling, in *Particle-Based Methods IV: Fundamentals and Applications: Fourth International Conference on Particle-Based Methods, Fundamentals and Applications (Particles), Barcelona, Spain, September 28–30, 2015*, edited by E. Oñate, M. Bischoff, D. R. J. Owen, P. Wriggers, and T. E. Zohdi (International Center for Numerical Methods in Engineering (CIMNE), Barcelona, Spain, 2015), pp. 558–566.
- [106] J. Bear, *Dynamics of Fluids in Porous Media* (Elsevier, New York, 1972).